

Journal of Fluid Mechanics

Date of delivery: September 21, 2018

Journal and vol/article ref: **flm** **1800726**

Number of pages (not including this page): 28

page 1 of 2

This proof is sent to you on behalf of Cambridge University Press.

Authors are strongly advised to read these proofs thoroughly because any errors missed may appear in the final published paper. This will be your ONLY chance to correct your proof. Once published, either online or in print, no further changes can be made.

Please return marked proofs **within 7 days** of receipt to: **JFMProofing@sunrise-setting.co.uk**

THIS PDF IS FOR PROOF CHECKING PURPOSES ONLY. IT SHOULD NOT BE DISTRIBUTED TO THIRD PARTIES AND MAY NOT REPRESENT THE FINAL VERSION.

CORRECTING AND RETURNING YOUR PROOFS – PLEASE READ

The proofs show changes made to the MAIN TEXT by the Copy Editor. Inserted text is shown in red. Locations of deleted text are indicated with a yellow rectangle/grey arrow. When viewed using the free Adobe Reader software, deleted text becomes visible when the pointer hovers over the yellow rectangle. (This does not happen with other PDF viewers.) **PLEASE DO NOT USE 'Mac OS X 10.9.3 Quartz PDFContext'** to save the pdf, it corrupts the proofs (known bug).

Do not attempt to edit the body of the text within the pdf in any way. □

PLEASE CHECK CAREFULLY **maths formulae** (changes cannot be tracked) and **figures/captions** (all are relabelled by the typesetter and should be checked against your originals).

HOW TO RETURN YOUR PROOFS

PLEASE DO NOT SEND LISTS - ALL CORRECTIONS AND NOTES MUST BE MARKED DIRECTLY ON THE PDF PROOFS AND BE CLEAR AND SUCCINCT. Emails are not passed on with the PDF. Please avoid lists, dialogue and long explanations.

You can mark up proofs either on screen using the enabled electronic editing tools or by hand on the hardcopy.

Marking up electronically. All proofs are enabled to allow electronic annotation in the free Adobe Reader software. Using your cursor select the text for correction, right click and use the most appropriate single tool (i.e. 'Replace', 'Cross out' or 'Add note to text'), to insert place the cursor then go to Tools/Comment&mark up/Text edits/Insert text at cursor. Please do not use the 'Sticky note' function its placement is not precise enough. 'Show comments' allows all marks to be clearly seen by the typesetter, please do not emphasise your marks in any way. Please return the file as an attachment via email.

Marking up by hand. Please use the proof correction symbols indicated keeping marks clear and concise. Scanned proofs can be returned via email.

Journal of Fluid Mechanics

Offprints: If you wish to order paper offprints, this should be done at the same time as returning your proofs. Please click on the link below to download an order form. Please follow the instructions on the form carefully and complete it as an electronic form if possible.

<https://www.cambridge.org/core/services/aop-file-manager/file/5aec57c3f6e65274069f35bc>

If you have no corrections to make please inform the Production Team by email - JFMProofing@sunrise-setting.co.uk

Postal address – to be used only where other options are not possible

Journal of Fluid Mechanics – Mrs A. R. James

Cambridge University Press

Edinburgh Building

Shaftesbury Road

Cambridge CB2 8RU, UK Tel: +44 (0)1223 326061

For further information about Journals Production please consult our FAQs at http://journals.cambridge.org/production_faqs

Please note:

- The proof is sent to you for correction of typographical errors only. Revision of the substance of the text is not permitted, unless discussed with the editor of the journal. Only **one** set of corrections are permitted.
- Please answer carefully any author queries.
- Corrections which do NOT follow journal style will not be accepted.
- A new copy of a figure must be provided if correction of anything other than a typographical error introduced by the typesetter is required.
- If you have problems with the file please contact

JFMproduction@cambridge.org

Please note that this pdf is for proof checking purposes only. It should not be distributed to third parties and may not represent the final published version.

Important: you must return any forms included with your proof.

Please do not reply to this email

NOTE - for further information about **Journals Production** please consult our **FAQs** at http://journals.cambridge.org/production_faqs

Proof correction symbols

Correction required	Marginal mark	Corresponding mark in text
Insert new material	Inserted material, followed by caret, 	
Delete		(Cross out what is not wanted)
Substitute new material for something typeset	Write new material followed by 	(Cross out material to be replaced)
Leave as printed	 under material to remain
Insert space		 where space is required
Take out space (close up)		 around material to be closed up
Insert hyphen		 where hyphen is required
Change letter(s) to capital(s)		 under letter(s) required
Change letter(s) to small capital(s)		 under letter(s) required
Change to small letter(s)		(Encircle required letter(s))
Change to bold type		 under letter(s) to be altered
Change to italic type		 under letter(s) to be altered
Begin a new paragraph		 before first word of new paragraph

Correction required	Marginal mark	Corresponding mark in text
No new paragraph		 between paragraphs
Inferior (subscript) letter, e.g. x		 if to be inserted; cross out incorrect letter if a replacement
Superior (superscript) letter, e.g. p		 if to be inserted; cross out incorrect letter if a replacement
Transpose letters or words		 between letters or words
Indicate letters set upside-down		(Encircle letters to be altered)
Broken letter; replace by similar but undamaged character		(Encircle letters to be altered)
Insert parentheses		 where parentheses required
Insert square brackets		 where square brackets required
Insert apostrophe		 where apostrophe required
Insert quotation marks		 where quotation marks required

Viscoplastic slender-body theory

D. R. Hewitt^{1,†} and N. J. Balmforth²

¹Department of Applied Mathematics and Theoretical Physics, University of Cambridge,
Wilberforce Road, Cambridge CB3 0WA, UK

²Department of Mathematics, University of British Columbia, Vancouver, BC, V6T 1Z2, Canada

(Received 12 April 2018; revised 16 August 2018; accepted 5 September 2018)

Q1

Q2

Q3

The theory of slow viscous flow around a slender body is generalized to the situation where the ambient fluid has a yield stress. The local flow around a cylinder that is moving along or perpendicular to its axis, and rotating, provides a first step in this theory. Unlike for a Newtonian fluid, the nonlinearity associated with the viscoplastic constitutive law precludes one from linearly superposing solutions corresponding to each independent component of motion, and instead demands a full numerical approach to the problem. This is accomplished for the case of a Bingham fluid, along with a consideration of some asymptotic limits in which analytical progress is possible. Since the yield stress of the fluid strongly localizes the flow around the body, the leading-order slender-body approximation is rendered significantly more accurate than the equivalent Newtonian problem. The theory is applied to the sedimentation of inclined cylinders, bent rods and helices, and compared with some experimental data. Finally, the theory is applied to the locomotion of a cylindrical filament driven by helical waves through a viscoplastic fluid.

Key words: biological fluid dynamics, low-Reynolds-number flows, non-Newtonian flows, plastic materials, propulsion, slender-body theory

1. Introduction

Slow viscous flow past a cylinder is a classical problem in fluid mechanics and is associated with Stokes' observation that there is no solution for a Newtonian fluid with zero Reynolds number in an infinite domain. The resolution of the Stokes paradox, which partly laid the foundation for the modern theory of matched asymptotic expansions (Hinch 1991), is that inertia must play a role sufficiently far from the cylinder (Lamb 1932). The viscoplastic version of the problem has been considered since the 1950s, with detailed numerical computations conducted by, for example, Roquet & Saramito (2003) and Tokpavi, Magnin & Jay (2008). The key feature of a viscoplastic fluid is its yield stress: material only flows like a fluid if the stresses exceed a critical yield threshold. The consequence for a cylinder moving through a viscoplastic fluid is that there is no motion if the force on the object is insufficient to yield the fluid. In a related manner, viscoplasticity is also expected to resolve the Stokes paradox without the need for inertia, since the stress decays away from the cylinder, and so sufficiently distant material must eventually become rigid.

[†] Email address for correspondence: drh39@cam.ac.uk

Previous studies of a cylinder moving through viscoplastic fluid have considered motion perpendicular to the axes. In the plastic limit (when the yield stress dominates the viscous stress, as must be the case close to the initiation of motion), this problem reduces to determining the critical load on a cylindrical pile embedded in cohesive soil, which was solved by Randolph & Houlsby (1984) using the method of sliplines. Our first aim in this current paper is to consider the more general situation of creeping viscoplastic flow around an infinitely long cylinder that translates at an arbitrary angle to its axis and can also rotate at an arbitrary rate. We achieve this by exploring analytically various asymptotic limits, and by providing full numerical solutions for the motion of a cylinder through a Bingham fluid inclined at an arbitrary angle. Note that, unlike for a Newtonian fluid, the **nonlinearity** inherent in the viscoplastic rheology prohibits the simple linear superposition of the independent cylinder motions to construct general solutions.

More broadly, our goal in this paper is to provide the viscoplastic analogue of slender-body theory for slow viscous flow (e.g. Keller & Rubinow 1976), for which the local flow around a cylinder provides a crucial stepping stone. The viscous theory underscores analyses of elongated particles or fibres in suspension (Tornberg & Shelley 2004) and the propulsion of micro-organisms by flagella (Taylor 1952; Hancock 1953; Lighthill 1975; Lauga & Powers 2009), the latter of which has also enjoyed generalization to motion through **granular** media (Hosoi & Goldman 2015). From a theoretical standpoint, the great advantage of a viscoplastic fluid is that flow past an object becomes **localized** to the vicinity of that object. Indeed, under the assumption that the **localization** around a cylindrical filament is sufficiently strong (i.e. the yield surfaces lie at distances of the order of the object's radius), and that it is sufficiently slender (i.e. its radii of curvature are much larger than its radius), the dynamics of the filament locally reduce to that of flow around a relatively long and straight cylinder. This reduction is equivalent to classical **resistive force theory** (Hancock 1953; Lighthill 1975; Gray & Hancock 1979), but is made much more effective here by the flow-localizing effect of the yield stress.

We apply the results of our analysis to two sets of problems. First, we consider the inertialess sedimentation of rods, that are either straight and inclined, or bent symmetrically into v-shapes. We extract the threshold for motion, together with the speed and direction of motion, for a given inclination angle and ratio of driving force and yield stress. We compare these theoretical predictions with the results of some simple experiments of sedimenting cylinders in **Carbopol** gel. We also compare with previous experimental studies of viscoplastic sedimentation and fractionation (Jossic & Magnin 2001; Madani *et al.* 2010).

Second, we explore the motion of a cylindrical filament that is twisted into a helix. We again examine how such an object falls under the action of a force, this time directed along the helix axis, and extract the fall speed and rotation rate for different helical pitch angles. Qualitative comparison is again made with a simple experiment of a sedimenting helix in **Carbopol** gel. We then apply our results to describe locomotion of a swimming helix, as in classical studies of biological locomotion through a Newtonian fluid (Taylor 1952; Hancock 1953). In this model, the helix is propelled forwards when it exerts a torque around its axis, forcing it to turn.

2. Slender-body formulation

2.1. Governing equations

Consider an infinitely long cylindrical filament moving through an incompressible Bingham fluid. We neglect gravity and inertia, and attach a local cylindrical polar

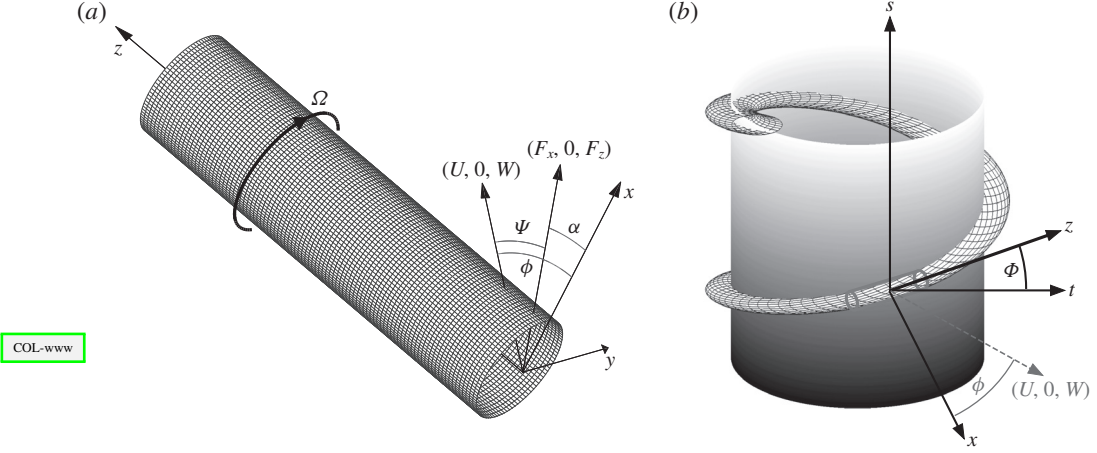


FIGURE 1. (Colour online) Sketch of the geometry: (a) the local cylindrical configuration. (b) A slender curved filament with circular cross-section wrapped around another cylinder to form a helix.

coordinate system (r, θ, z) to the body, as illustrated in figure 1(a). The cylinder translates at velocity $U\hat{x} + W\hat{z}$ and rotates around its axis with angular velocity $\tilde{\Omega}$. Under the assumption that axial variation in the flow field is weak and can be ignored, the dimensionless governing equations for the fluid velocity in cylindrical polar coordinates $(u(r, \theta), v(r, \theta), w(r, \theta))$ and pressure $p(r, \theta)$ are

$$\frac{1}{r} \frac{\partial}{\partial r}(ru) + \frac{1}{r} \frac{\partial v}{\partial \theta} = 0, \quad (2.1)$$

$$\frac{\partial p}{\partial r} = \frac{1}{r} \frac{\partial}{\partial r}(r\tau_{rr}) + \frac{1}{r} \frac{\partial}{\partial \theta} \tau_{r\theta} - \frac{\tau_{\theta\theta}}{r}, \quad \frac{1}{r} \frac{\partial p}{\partial \theta} = \frac{1}{r^2} \frac{\partial}{\partial r}(r^2\tau_{r\theta}) + \frac{1}{r} \frac{\partial}{\partial \theta} \tau_{\theta\theta}, \quad (2.2a,b)$$

$$0 = \frac{1}{r} \frac{\partial}{\partial r}(r\tau_{rz}) + \frac{1}{r} \frac{\partial}{\partial \theta} \tau_{\theta z}, \quad (2.3)$$

where τ_{ij} is the deviatoric stress tensor, and subscripts indicate tensor components. The Bingham law relates the stress to the strain rate $\dot{\gamma}_{ij}$,

$$\tau_{ij} = \left(1 + \frac{Bi}{\dot{\gamma}}\right) \dot{\gamma}_{ij} \quad \text{for } \tau > Bi, \quad (2.4)$$

and $\dot{\gamma}_{ij} = 0$ otherwise. Here, the strain rate is related to the velocity field by

$$\{\dot{\gamma}_{ij}\} = \begin{pmatrix} 2u_r & v_r + (u_\theta - v)/r & w_r \\ v_r + (u_\theta - v)/r & 2(v_\theta + u)/r & w_\theta/r \\ w_r & w_\theta/r & 0 \end{pmatrix}, \quad (2.5)$$

where subscripts of r and θ on the velocity components denote partial derivatives, and $\dot{\gamma} = \sqrt{(\sum_{ij} \dot{\gamma}_{ij} \dot{\gamma}_{ij})/2}$ and $\tau = \sqrt{(\sum_{ij} \tau_{ij} \tau_{ij})/2}$ denote the tensor second invariants. We incorporate the incompressibility condition directly by defining a streamfunction $\psi(r, \theta)$ such that $u = r^{-1} \partial \psi / \partial \theta$ and $v = -\partial \psi / \partial r$.

To arrive at this dimensionless system, we use the radius of the filament, \mathcal{R} , and the translation speed of the cylinder, $\mathcal{U} = \sqrt{U^2 + W^2}$, to remove the dimensions of length and velocity, respectively, while the stresses and pressure are scaled by $\mu\mathcal{U}/\mathcal{R}$, where μ is the (plastic) viscosity. These scalings introduce the Bingham number,

$$Bi = \frac{\tau_Y \mathcal{R}}{\mu \mathcal{U}}, \quad (2.6)$$

where τ_Y is the yield stress.

With this scaling of the variables, the cylinder translates in the (x, z) -plane with unit dimensionless speed at an angle ϕ to the x axis; the Cartesian translation velocity is $\cos \phi \hat{x} + \sin \phi \hat{z}$ (see figure 1a). The cylinder also rotates around its axis with the dimensionless rotation rate $\Omega \equiv \tilde{\Omega} \mathcal{R} / \mathcal{U}$. Consequently, we impose

$$(u, v, w) = (\cos \theta \cos \phi, \Omega - \sin \theta \cos \phi, \sin \phi) \quad \text{at } r = 1. \quad (2.7)$$

In the far field, the stresses must eventually fall below the yield stress and the fluid must plug up, such that $(u, v, w) \rightarrow (0, 0, 0)$. We exploit this fact to introduce a finite computational domain in which we set $(u, v, w) = (0, 0, 0)$ at an outer radius $r = R_o$. Provided this boundary lies well beyond the yield surface, we expect that its precise location has no effect. Importantly, when $Bi = O(1)$ the yield surfaces are expected to occur at radii of order one, underscoring the strong localizing effect of the yield stress on the flow around the cylinder and rendering accurate the leading-order approximation of slender-body theory.

2.2. Forces and torque

On the surface of the cylinder ($r = 1$), the fluid exerts the force $(\tau_{rr}, \tau_{r\theta}, \tau_{rz})|_{r=1}$. This leads to a net drag per unit length of $\hat{x}F_x + \hat{z}F_z$, with

$$\begin{bmatrix} F_x \\ F_z \end{bmatrix} = \oint \begin{bmatrix} (-p + \tau_{rr}) \cos \theta - \tau_{r\theta} \sin \theta \\ \tau_{rz} \end{bmatrix}_{r=1} d\theta = \oint \begin{bmatrix} 2\tau_{rr} \cos \theta + (r\tau_{r\theta})_r \sin \theta \\ \tau_{rz} \end{bmatrix}_{r=1} d\theta, \quad (2.8)$$

where the latter expression follows from an integration by parts, and provides a convenient form for calculation of the forces without first calculating the pressure field. If the cylinder rotates ($\Omega \neq 0$), there is also a torque given by

$$T = r^2 \oint \tau_{r\theta}(r, z) d\theta. \quad (2.9)$$

The force balance (and, in particular, the integral of (2.2b) in θ) demands that T is independent of r .

The two drag components, $F_x(\phi, \Omega, Bi)$ and $F_z(\phi, \Omega, Bi)$, and torque, $T(\phi, \Omega, Bi)$, are the key ingredients when fully formulating slender-body theory. For the applications in § 4, we consider straight or bent rods, or a helix, and the net force and torque on these objects follow immediately from $F_x(\phi, \Omega, Bi)$, $F_z(\phi, \Omega, Bi)$ and $T(\phi, \Omega, Bi)$. The remaining step in applying the slender-body theory is to ensure that the object is either **force free** in a certain direction or **torque free**, which ultimately prescribes either the translation direction, rotation rate or swimming speed.

For a slender body with a twisted **centreline**, the drag force and torque vary with position along the **centreline**. Integrating these quantities over the arc length then provides an estimate for the total force and torque acting on the body. This leading-order calculation corresponds to the resistive force theory of viscous fluid mechanics, which is often considered to be a poor approximation in view of **non-local** logarithmic corrections to the viscous-flow solution due to the finite aspect ratio of the body (e.g. Lauga & Powers 2009). Here, no such logarithmic corrections are expected because of the localization of the flow by the yield stress, provided that Bi is not small and there are no significant effects stemming from the ends of the object.

2.3. Some numerical details

We solve the equations numerically using an extension of the augmented Lagrangian scheme described by Hewitt & Balmforth (2017). The key extension here is to combine the Stokes-like solver used there for the streamfunction with a similar (but lower-order) scheme for the axial velocity w . These equations reduce in the Newtonian limit to a biharmonic equation for ψ and Laplace's equation for w ; for non-zero Bingham number, the equations are instead solved iteratively. We omit further details of the augmented Lagrangian scheme, which have been described in numerous previous studies (e.g. Saramito & Wachs 2017).

Given Bi , ϕ and Ω , the equations are solved by adopting truncated Fourier series for the angular dependences and using standard second-order finite differences in the radial direction, giving a band-diagonal matrix problem. When $\Omega = 0$, solutions can be computed directly by matrix inversion. When $\Omega \neq 0$, however, and as a consequence of working with a streamfunction rather than with pressure, we cannot directly impose the constraint that the torque T is independent of radius (see (2.9)). Instead, we enforce the constraint by iterating the net azimuthal flux around the cylinder until the radial variation in the calculated torque falls below a tolerance of 0.5%. The resultant nested iterative scheme is qualitatively similar to that employed by Hewitt & Balmforth (2017) to enforce a condition of zero net force in a related problem.

3. Breaking the problem down

The problem outlined in §2 can be broken down into pieces to understand its constituents in more detail, although the nonlinearity of the viscoplastic flow law forbids us from simply superposing these pieces to build general solutions. These pieces correspond to some idealized examples that have received attention in the existing literature, as well as some that have not, and lead to some special limits in which analytical progress is possible to build asymptotic or exact solutions.

3.1. Newtonian limit

In the limit $Bi \rightarrow 0$, the yield stress becomes unimportant over the regions near the cylinder where the viscous stresses remain high. Only further away do those stresses decline to permit viscoplasticity to affect the flow. Thus, the solution is composed of a near-field Newtonian region and a far-field viscoplastic one. Despite this, the Newtonian solution is controlled by the far-field conditions, owing to the presence of logarithmically diverging corrections. In this manner, the problem is directly analogous

to the removal of the classical Stokes paradox, with viscoplasticity here taking the role of inertia.

Over the Newtonian region we may compute a solution perturbatively by adopting asymptotic solutions in the sequence $1, (\log Bi^{-1})^{-1}, \dots$, as in the classical problem of Stokes flow past a cylinder (e.g. Hinch 1991). The leading two orders, $\psi \sim \psi_0 + (\log Bi^{-1})^{-1}\psi_1$ and $w \sim w_0 + (\log Bi^{-1})^{-1}w_1$ satisfy the Newtonian problems, $\nabla^4\psi_0 = \nabla^4\psi_1 = \nabla^2w_0 = \nabla^2w_1 = 0$, subject to the no-slip conditions on the cylinder. The remaining arbitrary constants in the solutions are fixed by demanding a match to the far-field solution where $r = O(Bi^{-1})$ and $(u, w) \rightarrow 0$. We thus find

$$\psi \sim \sin\theta \cos\phi \left[r - \frac{2r \log r - r + r^{-1}}{2 \log Bi^{-1}} \right] - \Omega \log r, \quad (3.1a)$$

$$w \sim \sin\phi \left(1 - \frac{\log r}{\log Bi^{-1}} \right), \quad (3.1b)$$

without any need to calculate explicitly the viscoplastic far-field structure. Given (3.1), the drag force and torque can be computed from (2.8)–(2.9) to be

$$\begin{bmatrix} F_x \\ F_z \end{bmatrix} \sim -\frac{2\pi}{\log Bi^{-1}} \begin{bmatrix} 2 \cos\phi \\ \sin\phi \end{bmatrix} \quad \text{and} \quad T \sim -4\pi\Omega. \quad (3.2a,b)$$

Note that the drag force and torque are decoupled in this limit: the drag is independent of the rotation rate Ω and the torque is independent of translation.

3.2. No transverse motion

If the cylinder moves with only axial translation (i.e. $\phi = \pi/2$) and rotation, some analytical progress is possible because the flow is independent of the polar angle θ . Integration of the force-balance equations (2.2b) and (2.3), together with the condition $\tau = Bi$ at the yield surface, gives expressions for the non-zero stress components,

$$(\tau_{rz}, \tau_{r\theta}) = -\frac{r_p}{r} Bi \left(C, S \frac{r_p}{r} \right) = \left(1 + \frac{Bi}{\dot{\gamma}} \right) (w_r, v_r - v/r), \quad (3.3)$$

where $\dot{\gamma}^2 = w_r^2 + (v_r - v/r)^2$ in this limit, and $(C, S) = (\cos \Upsilon, \sin \Upsilon)$, with Υ a parameter defined such that the yield surface is the circle $r = r_p$. The drag and torque are thus

$$F_x = 0, \quad F_z = -2\pi r_p C Bi, \quad T = -2\pi r_p^2 S Bi, \quad (3.4a-c)$$

from (2.8) and (2.9). Given that $w = v = 0$ at $r = r_p$, the integral of (3.3) gives the velocity components,

$$w = \frac{r_p Bi}{C} \left[C^2 \log \left(\frac{r_p}{r} \right) - 1 + \sqrt{S^2 + C^2 (r/r_p)^2} \right] \quad (3.5)$$

and

$$v = \frac{r Bi}{2} \left\{ S \left(\frac{r_p^2}{r^2} - 1 \right) + \ln \left[\frac{(1+S)(\sqrt{C^2 + S^2 (r/r_p)^2} - S)}{(1-S)(\sqrt{C^2 + S^2 (r/r_p)^2} + S)} \right] \right\}. \quad (3.6)$$

218 Finally, the parameter Υ and location of the yield surface $r = r_p$ follow from the
 219 implicit relations implied by the boundary conditions in this limit, $w = 1$ and $v = \Omega$
 220 at $r = 1$.

221 For large yield stress, $Bi \gg 1$, the yield surface approaches the surface of the
 222 cylinder and we arrive at the relations,

$$223 \quad (w, v) \sim (1, \Omega) \left(\frac{r_p - r}{r_p - 1} \right)^2 \quad \text{and} \quad (F_z, T) \sim -2\pi Bi(C, S), \quad (3.7a,b)$$

224 with

$$225 \quad \Omega \sim \tan \Upsilon \quad \text{and} \quad r_p \sim 1 + \sqrt{2}[(1 + S^2)CBi]^{-1/2}. \quad (3.8a,b)$$

226 Thus the region of flow around the cylinder is **localized** to a narrow layer of width
 227 $O(Bi^{-1/2})$ when $Bi \gg 1$. If also $\Omega \gg 1$, the thickness of that yielded annulus increases
 228 like $O(\Omega^{1/2})$, while the axial drag force decreases like $O(\Omega^{-1})$ and the torque
 229 approaches $T \sim -2\pi Bi$. That is, unlike in the Newtonian limit discussed above,
 230 rotating the cylinder in the plastic limit reduces the drag.

231 Conversely, for small yield stress, $Bi \ll 1$, the location of the yield surface r_p
 232 becomes large and the parameter Υ becomes small:

$$233 \quad r_p \sim \frac{1}{Bi \log Bi^{-1}} \quad \text{and} \quad S \sim 2\Omega Bi(\log Bi^{-1})^2. \quad (3.9a,b)$$

234 This leads to the force F_z and torque T quoted in (3.2) with $\phi = \pi/2$.

235 In the absence of rotation ($\Omega = 0$), the solution is more explicit:

$$236 \quad w = 1 + Bi(r - 1 - r_p \log r) \quad \text{and} \quad Bi^{-1} = 1 - r_p + r_p \log r_p, \quad (3.10a,b)$$

237 which, for $Bi \gg 1$, **gives** $r_p \rightarrow 1 + \sqrt{2}Bi^{-1/2}$, $w \rightarrow (1 - \xi)^2$ and $F_z \sim -2\pi Bi$, where
 238 $\xi = (r - 1)Bi^{1/2}/\sqrt{2}$.

239 3.3. No axial motion

240 3.3.1. Pure transverse motion

241 In the absence of axial motion ($\phi = 0$), the problem reduces to two-dimensional
 242 flow around a circle. This limit without rotation was discussed at length by Tokpavi
 243 *et al.* (2008). In general, the two-dimensional structure of the flow field in this limit
 244 precludes analytical progress except in the limits of small or large Bi .

245 Sample numerical solutions with no rotation ($\Omega = 0$) are shown in figure 2,
 246 together with a collection of data that highlight how certain flow features vary with
 247 the Bingham number. The density plots in the figure show $\log_{10} \dot{\gamma}$, with the **plug**
 248 regions in black and superposed streamlines (i.e. $\psi = \text{constant}$) in the frame of the
 249 ambient fluid. As Bi is increased, flow becomes more localized to the cylinder, but
 250 unlike in the problem without translation, the fluid remains yielded over a region
 251 of $O(1)$ -extent, even as $Bi \rightarrow \infty$ (figure 2d). Over the bulk of those regions, shear
 252 rates are low but finite and the fluid deforms in the manner of ideal plasticity:
 253 two triangular plugs remain attached to the front and back of the cylinder, and
 254 rigidly rotating cells survive at the centre of the plastic zones. The plastic zones are
 255 buffered from the cylinder and plugs by high-shear boundary layers within which
 256 viscous stresses remain important. As illustrated in figure 2(e), the width of these

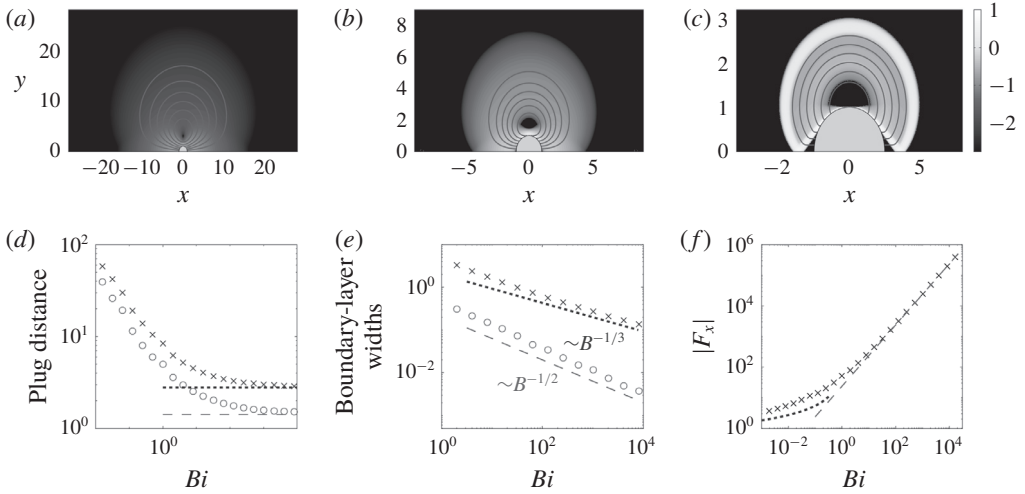


FIGURE 2. (Colour online) (a–c) Density plots of the logarithmic strain rate $\log_{10}(\dot{\gamma})$ in the (x, y) -plane (showing only $y > 0$), for a cylinder translating in the x direction ($\phi = 0$), with (a) $Bi = 0.0625$, (b) $Bi = 1$ and (c) $Bi = 1024$ (note the different axis scales). The (blue) curves show streamlines, $\psi = \text{constant}$, in the frame of the ambient fluid. (d) The distance from the centre of the cylinder to the furthest yield surface along the x (red circles) and y (blue crosses) axes; the slipline predictions ($\sqrt{2}$ and $2 + (\pi/4)$) are shown by dashed lines. (e) The widths of the boundary layer against the cylinder (red circles) and the outer free shear layer (blue crosses), both along $x = 0$. (f) The force $|F_x(Bi)|$, together with the Newtonian (blue dots; (3.2a)) and plastic (red dashed; (3.11)) predictions.

boundary layers **decreases** with the Bingham number, in agreement with viscoplastic boundary-layer theory (appendix A; see also Balmforth *et al.* (2017)).

The solution for the plastic zones can be constructed using the method of characteristics, or slipline theory; see Randolph & Houlsby (1984). In this construction, there are two families of orthogonal characteristic curves, the sliplines, whose local tangents make angles of ϑ and $(\pi/2) + \vartheta$ with the x -axis. The curves are normally referred to as either α or β lines, and have the Riemann invariants, $p \pm 2Bi\vartheta$. As illustrated in figure 3(a), Randolph and Houlsby’s slipline construction proceeds by placing centred semicircular fans of the characteristics of radius $1 + (\pi/4)$ at the points $(0, \pm 1)$. These fans are then extended immediately below or above by continuing the circular arcs as the involutes of other circles and adding new straight sliplines that meet the cylinder tangentially (i.e. the fans become non-centred and follow the cylinder surface). The plastic regions are terminated by straight sliplines of unit slope that meet at $(x, y) = (\pm\sqrt{2}, 0)$.

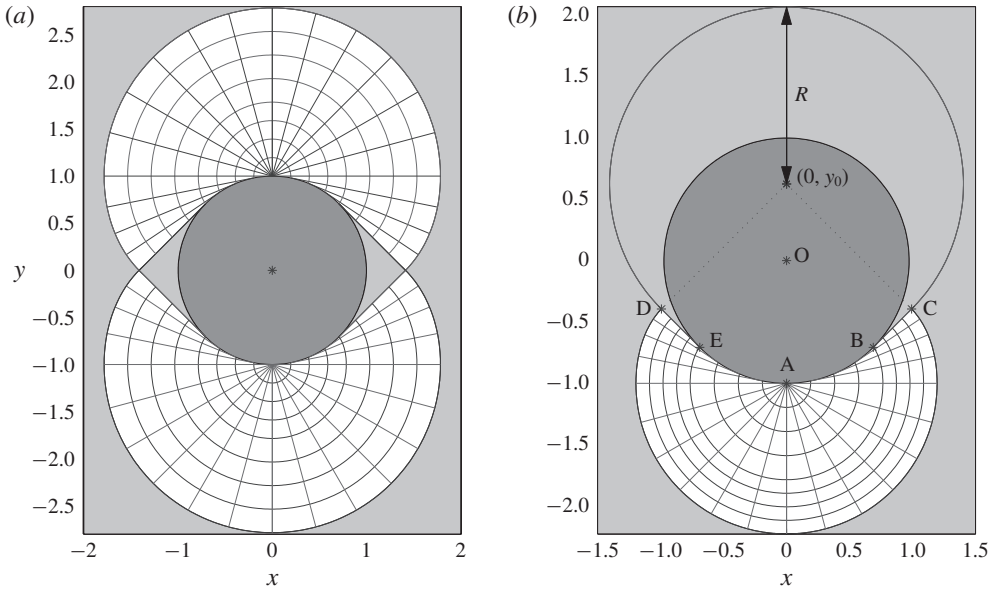
The slipline stress solution predicts that

$$F_x = -4(\pi + 2\sqrt{2})Bi, \quad (3.11)$$

as $Bi \rightarrow \infty$ (Randolph & Houlsby 1984). The drag force F_x for general Bi is plotted in figure 2(f), and recovers the slipline prediction for $Bi > 10$ or so.

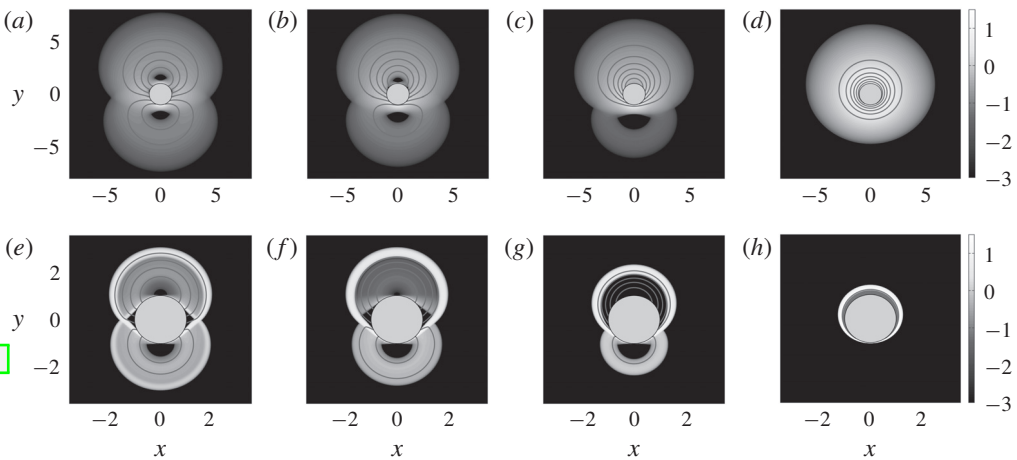
3.3.2. Transverse motion and rotation

Sample solutions with both transverse motion and rotation are shown in figure 4; corresponding results for the drag force and torque are presented in figure 5. The



COL-www

FIGURE 3. (Colour online) Slipline solutions for (a) $\Omega = 0$ and (b) $\Omega = 1.6$. The two families of sliplines are shown with different colours (α -lines are red; β -lines are blue). Plugs are shaded light grey.



COL-www

FIGURE 4. (Colour online) Density plots of $\log_{10} \dot{\gamma}$ on the (x, y) -plane, overlain by streamlines, for a cylinder translating with unit velocity in the x direction ($\phi = 0$) and rotating with angular velocity (a,e) $\Omega = 0.4$, (b,f) $\Omega = 0.8$, (c,g) $\Omega = 1.6$ and (d,h) $\Omega = 12.8$. The upper row (a–d) is for $Bi = 1$; the lower row (e–h) is for $Bi = 2048$.

278 inclusion of rotation desymmetrizes the velocity field about the x -axis, strengthening
 279 the recirculating cell above the cylinder (for anti-clockwise rotation) and weakening
 280 that below. Eventually, for sufficiently large Ω , the lower cell disappears, which, for
 281 $Bi \gg 1$, leaves a thin boundary layer coating the cylinder.

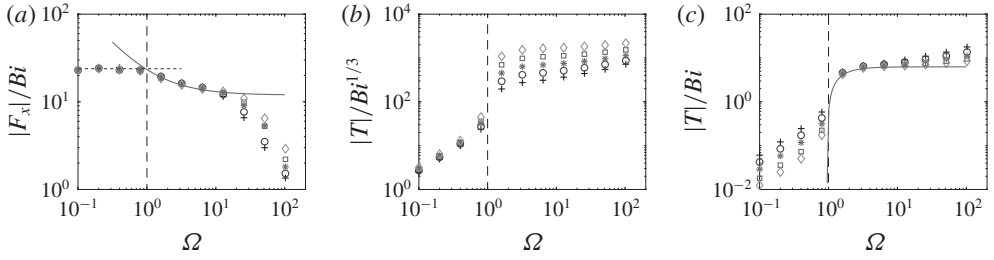


FIGURE 5. (Colour online) (a) Force and (b,c) torque for a cylinder translating with unit velocity in the x direction ($\phi = 0$) and rotating with angular velocity Ω . The data are scaled as indicated. The vertical dashed lines mark $\Omega = 1$. Other lines show predictions for $Bi \gg 1$: the horizontal dashed line in (a) shows the force for pure translation (3.11), and the red solid lines show the force and torque for solutions with a rigidly rotating upper plug (3.12). The different colours/symbols indicate data for $Bi = 2^n$ with $n = 8$ (black cross), $n = 9$ (blue circle), $n = 10$ (red star), $n = 11$ (green square) and $n = 12$ (grey diamond).

In the limit $Bi \gg 1$, it is again possible to construct slipline solutions bordered by viscoplastic boundary layers. For sufficiently small Ω the rotation of the cylinder has no effect on the stress field, leaving a slipline pattern equivalent to the non-rotating case, but with an asymmetrical velocity field; see figure 4(a). An immediate consequence is that, to leading order in Bi^{-1} , the drag force remains as in (3.11) and, because the torque vanishes for $\Omega = 0$, $T \ll O(Bi)$. In fact, the numerical results indicate that $T = O(Bi^{1/3})$ over this range of Ω (see figure 5b), highlighting its origin within the viscoplastic boundary layers.

For large Bi , the $\Omega = 0$ stress solution is eventually replaced by a second, alternative stress pattern for higher Ω in which a rigidly rotating plug attached to the cylinder takes the place of the upper fan. The alternative pattern is feasible because the no-slip condition on the cylinder, with velocity field $\hat{x} + \Omega(y\hat{x} + x\hat{y})$, can be accommodated by rigid rotation about a centre $(0, y_0)$, with $y_0 = \Omega^{-1}$. The rigidly rotating plug demands a circular arc of failure, which broadens into a viscoplastic shear layer in the Bingham computation of figure 4(g). The broadened arc merges with the viscoplastic boundary layer underneath the cylinder, leaving intact an underlying plastic zone. The stress solution makes the transition between the two patterns over a window of rotation rates around $\Omega = 1$ (see e.g. figure 4f,g), with the second stress pattern becoming accessible once the centre of rotation $y_0 = \Omega^{-1}$ lies close to or inside the cylinder.

The slipline solution corresponding to the alternative stress-field pattern is illustrated in figure 3(b). The upper circular failure arc must correspond to a slipline in ideal plasticity, and therefore continues one of the straight sliplines that leave tangentially from the lower half of the cylinder. This in turn is met by other sliplines to join the fan underneath the cylinder, which persists in the re-organization of the plastic flow. The requirement that there is no net pressure drop around the sliplines that border the region of deformation (i.e. the union of the circular failure arc and the outer periphery of the fan) demands that the fan and circular failure arc intersect along sliplines that make angles of $\pm(\pi/4)$ with the x -axis (BC and DE in figure 3b). It follows from geometrical considerations that the radius of the rigidly rotating plug is $R = 1 + y_0/\sqrt{2}$. Further details of this slipline construction can be found in appendix B. Moreover, a calculation using the resultant slipline stress-field solution, also outlined in appendix B,

gives

$$F_x = -Bi \left[2\pi + 4\sqrt{2} + \frac{(2+3\pi)}{\Omega} \right], \quad T = -\frac{1}{2}Bi \left[4\pi - \frac{(3\pi+2)}{\Omega^2} \right] \quad (3.12a,b)$$

and $F_z = 0$, for $Bi \gg 1$.

As Ω is increased still further, the rigidly rotating slipline pattern persists until the circular failure arc approaches the cylinder and the plug becomes consumed by the adjacent viscoplastic boundary layer (figure 4*h*). At this stage, the torque approaches the limit $-2\pi Bi$ expected for pure rotation. Simultaneously, the drag force abruptly falls off, see figure 5(*a*), for $\Omega \lesssim 20$. The residual drag stems from a ‘squeeze’ flow driven by the translation of the cylinder inside the rotationally induced boundary layer: continuity demands that the radial velocity of the cylinder forces an $O((r_p - 1)^{-1})$ correction to the angular velocity with an associated shear stress of $O((r_p - 1)^{-2})$. The radial derivative of this stress must be balanced by an angular pressure gradient, giving $p \sim O((r_p - 1)^{-3})$. Finally, because the boundary layer has thickness $r_p - 1 \sim O(Bi^{-1/2}\Omega^{1/2})$ (see § 3.2), and in view of (2.8), we find $F_x \sim O(\Omega^{-3/2}Bi^{3/2})$ for $\Omega \gg 1$.

4. Cylinders, rods and helices

4.1. Angled motion of a cylinder

A collection of numerical solutions for viscoplastic flow around a cylinder for varying B and ϕ are shown in figure 6. In these non-rotating solutions, the yield stress increases from left to right, and the orientation of motion with respect to the cylinder axis (ϕ) from top to bottom. The plots show density maps of $\log_{10} \dot{\gamma}$, overlain by streamlines in the (x, y) -plane (upper half) and contours of axial velocity w (lower half). The location of the yield surfaces for these and other solutions are shown in figure 7, while figure 8 shows results for the drag forces on the cylinder.

Figure 6(*a,h*) shows that solutions are relatively insensitive to the flow angle over a large range of ϕ . Indeed, the stress pattern of the solutions broadly mirrors that for pure transverse motion ($\phi = 0$; § 3.3.1). This behaviour is clearest for $Bi \gg 1$, where the outer yield surface remains close to the transverse limit over most of the range of ϕ (figure 7*c*), and only decreases towards the for the much smaller axial limit when ϕ becomes close to $\pi/2$. The persistence of this stress pattern reflects how the addition of axial motion for $\phi \ll 1$ constitutes a regular perturbation of the transverse-motion problem: the axial velocity w and associated axial drag F_z scale with ϕ in this limit, but the feedback on the transverse flow and transverse drag F_x (which occurs through the constitutive law and $\dot{\gamma}$) is $O(\phi^2)$.

For ϕ closer to $\pi/2$, however, the flow pattern adjusts more noticeably, and rather abruptly for $(\pi/2) - \phi = O(Bi^{-1})$ in the plastic limit $Bi \gg 1$. In this limit, the axial flow becomes restricted to a boundary layer against the cylinder, surrounded by a delocalized transverse flow with much weaker deformation rates characteristic of an almost perfectly plastic region (see figure 6*i*). The outer plastic flow persists very close to $\phi = \pi/2$, supporting a finite transverse drag F_x that exceeds the axial drag F_z even when the cylinder’s motion is almost aligned with its axis (figure 8*c*). Only for $(\pi/2) - \phi = O(Bi^{-1})$ does F_x eventually drop to zero (figure 8*d*). Some analysis of this limit is provided in appendix C.

The disparity between F_x and F_z for $(\pi/2) - \phi \gg O(Bi^{-1})$ leads to a drag anisotropy that becomes embedded in the variation of the orientation angle α of the force (figure 8*b*). This angle remains small (less than $\sim \pi/7$) over most of the range of ϕ ,

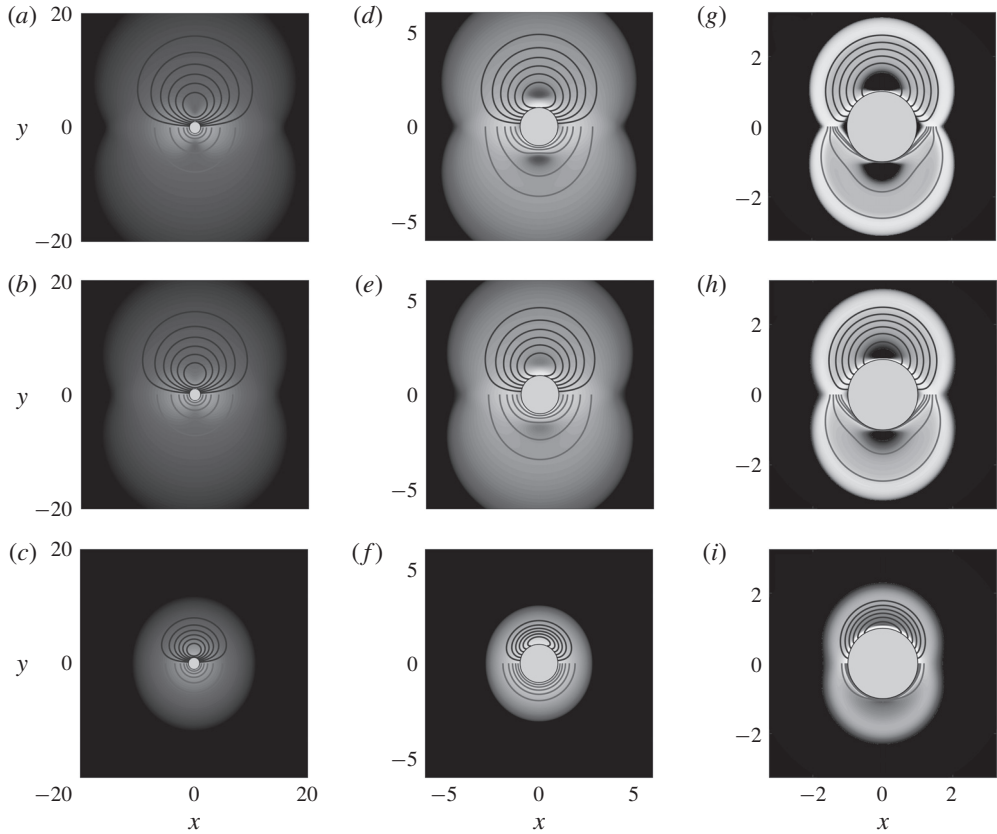


FIGURE 6. (Colour online) Density plots of logarithmic strain rate $\log_{10}(\dot{\gamma})$ for flow around non-rotating cylinders moving at an angle ϕ , together with streamlines in the (x, y) plane (i.e. $\psi = \text{constant}$; blue, shown for $y > 0$) and contours of the axial velocity w (green, shown for $y < 0$). From left to right, the yield stresses are (a–c) $B = 0.0625$, (d–f) $B = 1$ and (g–i) $B = 256$. From top to bottom, the angle of motion is (a,d,g) $\phi = \pi/8$, (b,e,h) $\phi = \pi/4$, and (c,f,i) $\phi = 19\pi/40$.

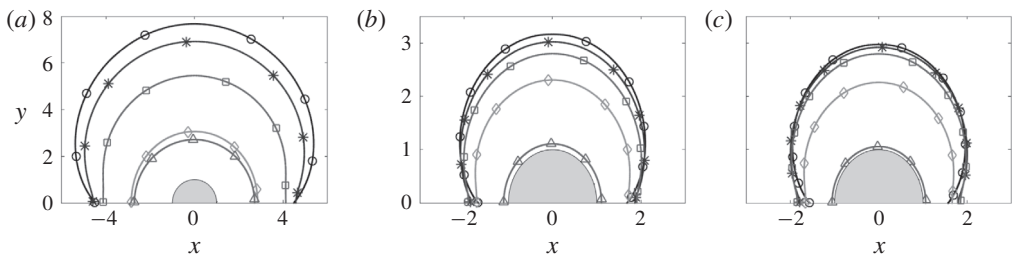


FIGURE 7. (Colour online) The outermost yield surface for (a) $Bi = 1$, (b) $Bi = 256$ and (c) $Bi = 2048$. The surfaces correspond to inclination angles of $\phi = 0$ (black, circles), $\phi = \pi/4$ (blue, stars), $\phi = 3\pi/8$ (green, squares), $\phi = 19\pi/40$ (grey, diamonds) and $\phi = \pi/2$ (red, triangles).

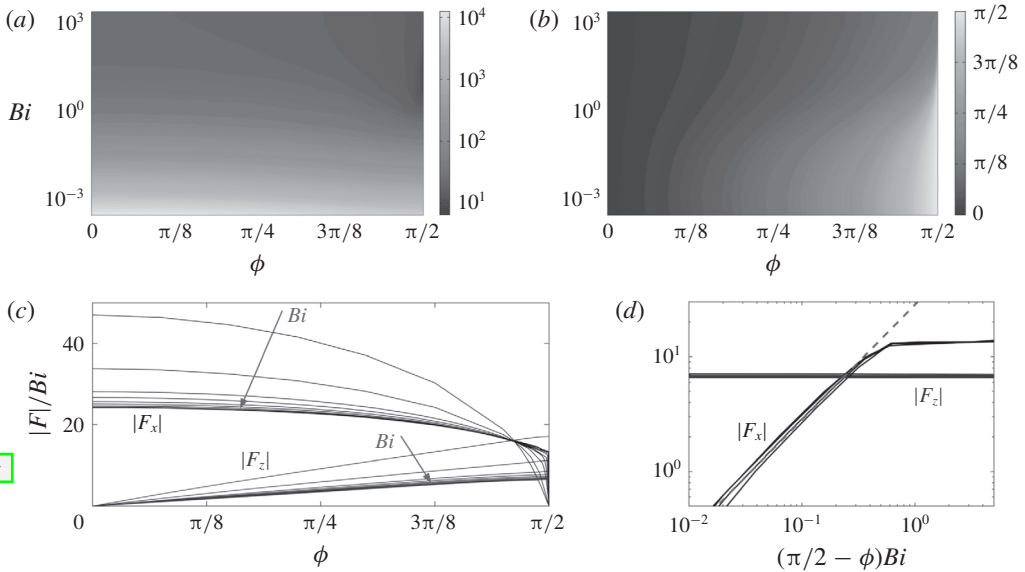


FIGURE 8. (Colour online) The drag force on a cylinder moving at an angle ϕ to the x -axis. (a) The magnitude of the force, scaled by the Bingham number, $|\mathbf{F}|/Bi$. (b) The orientation of the force relative to the x -axis $\alpha = \tan^{-1}(F_z/F_x)$. Note that larger values of α are confined to an increasingly narrow boundary layer for $Bi \gg 1$. (c) The components of the drag F_x/Bi (black) and F_z/Bi (blue) for $1 \leq Bi \leq 2^{10}$. (d) A magnification of the same data (showing $2^6 \leq Bi \leq 2^{10}$), for $\phi \rightarrow \pi/2$. The red dashed line shows $|F_x| = 9\pi(\pi/2 - \phi)Bi^2$ (see appendix C).

358 but increases sharply near $\phi = \pi/2$ where the transverse force F_x drops sharply.
 359 Consequently, in situations where the angle of the force is prescribed rather than the
 360 direction of motion, as in the examples that will be described presently, any variation
 361 in α must be accommodated by a sensitive tuning of ϕ near $\pi/2$: it is only when
 362 $\alpha \lesssim \pi/7$ that ϕ can vary over its full range.

363 4.2. Sedimentation of rods

364 4.2.1. An inclined straight rod

365 Consider a straight rod falling under the action of a force such as gravity. The force
 366 makes an angle of $(\pi/2) - \alpha$ with the cylinder axis (i.e. the z -direction; see figure 1a).
 367 The drag $\mathbf{F} = F_x \hat{\mathbf{x}} + F_z \hat{\mathbf{z}}$ must therefore also point in this direction to balance the
 368 applied force. Thus the angle $\alpha = \tan^{-1}(F_z/F_x)$ and magnitude $|\tilde{\mathbf{F}}|$ are specified in this
 369 problem, rather than the angle ϕ and speed \mathcal{U} of the resulting motion. It is therefore
 370 more natural to define a yield-stress parameter based on the dimensional applied line
 371 force $|\tilde{\mathbf{F}}|$ (e.g. the weight per unit length), rather than our previously defined Bingham
 372 number $Bi = \tau_Y \mathcal{R}/(\mu \mathcal{U})$. More specifically, we define an Oldroyd number

$$373 \quad Od = \frac{Bi}{|\mathbf{F}|} = \frac{\tau_Y \mathcal{R}}{|\tilde{\mathbf{F}}|}. \quad (4.1)$$

374 Then, given the switch in the specified physical parameters, we must translate our
 375 results by a suitable two-dimensional interpolation from the (ϕ, Bi) -parameter plane

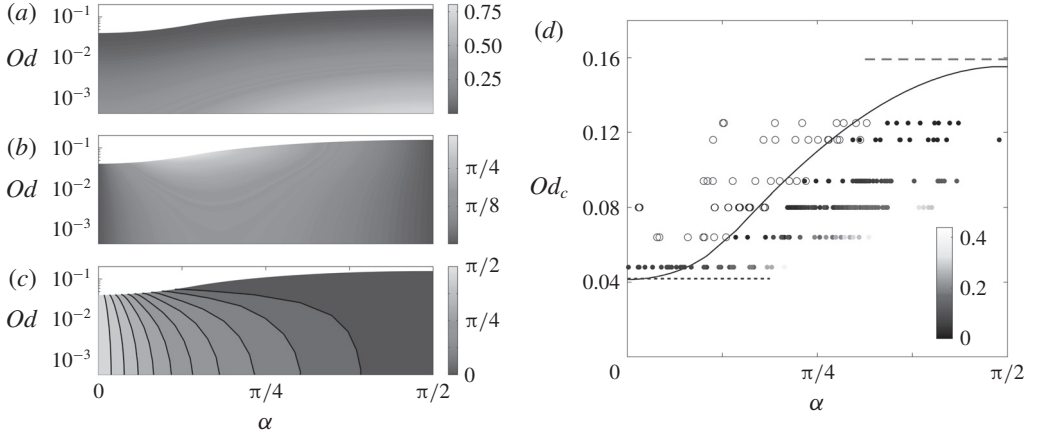


FIGURE 9. (Colour online) Numerical solutions for a cylinder whose axis is inclined at an angle of $(\pi/2) - \alpha$ to an applied force, with strength gauged by the Oldroyd number Od : (a) the fall speed V ; (b) the angle of motion $\Psi = \phi - \alpha$ relative to the applied force; and (c) the angle of motion $\pi/2 - \phi$ relative to its own axis. For $Od > Od_c(\alpha)$, the force on the cylinder is not sufficient to yield the fluid and there is no motion, leading to the white areas at the top of the plots. The critical value $Od_c(\alpha)$ is shown in (d), together with the limits of transverse (short blue dashed) and axial (long red dashed) orientation, and a set of experimental data for headless machine screws sedimenting through a Carbopol gel (see appendix D). Stationary rods are indicated by open circles and moving rods by filled circles, and the shading represents \sqrt{V} (in $\sqrt{\text{cm s}^{-1}}$), according to the colour scheme indicated.

to the new parameters, $(\alpha, Od) \equiv (\tan^{-1}(F_z/F_x), Bi/\sqrt{F_x^2 + F_z^2})$. We thereby arrive at the dimensionless fall speed V and angle Ψ to the force direction:

$$V(\alpha, Od) = \frac{\mu \mathcal{U}}{|\tilde{\mathbf{F}}|} \equiv \frac{Od}{Bi(\alpha, Od)} \quad \text{and} \quad \Psi(\alpha, Od) = \phi(\alpha, Od) - \alpha. \quad (4.2a,b)$$

These quantities are plotted in figure 9(a,b). As $Od \rightarrow 0$, the weight of the cylinder becomes much larger than the yield strength of the material and solutions approach the Newtonian limit, with limiting drag components $(F_x, F_z) = |\mathbf{F}|(\cos \alpha, \sin \alpha) \sim 2\pi(2 \cos \phi, \sin \phi)/\log Bi^{-1}$ (see (3.2)). The fall speed and angle thus approach

$$V \sim \frac{\log Od^{-1}}{4\pi} \sqrt{1 + 3 \sin^2 \alpha} \quad \text{and} \quad \Psi \sim \tan^{-1}(2 \tan \alpha) - \alpha, \quad (4.3a,b)$$

for $Od \rightarrow 0$.

Conversely, above a critical threshold value Od_c (figure 9d) the cylinder cannot exert sufficient stress on the material to move, and so remains stationary. This threshold value increases with orientation angle α , and lies between two limiting values for transverse ($\alpha = 0$) and axial ($\alpha = \pi/2$) sedimentation. These can be calculated for $Bi \gg 1$ from the asymptotic values of the force components in (3.7) and (3.11),

$$Od_c = \frac{Bi}{|\mathbf{F}|} \rightarrow \begin{cases} (4\pi + 8\sqrt{2})^{-1} & \alpha \rightarrow 0 \\ (2\pi)^{-1} & \alpha \rightarrow \pi/2. \end{cases} \quad (4.4)$$

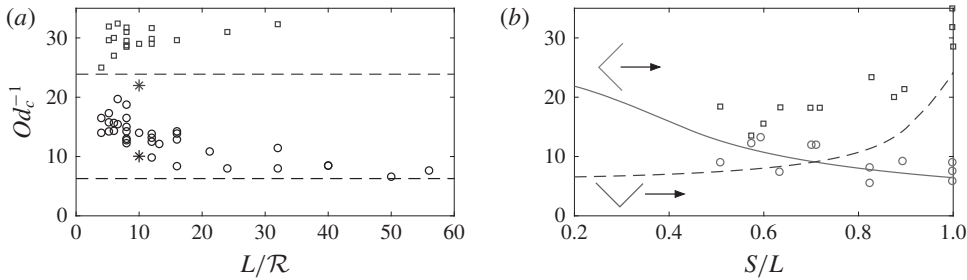


FIGURE 10. (Colour online) Comparison of experimental data from Madani *et al.* (2010) (points) with theory (lines) for the critical dimensionless force $1/Od_c$ at which cylinders of aspect ratio (length/radius) L/\mathcal{R} start to move. (a) Straight cylinders with axis aligned with the force (black circles) or side on to the force (blue squares) together with our corresponding predictions for an infinite cylinder (dashed lines). The corresponding experimental results of Jossic & Magnin (2001) are also shown by stars. (b) Bent cylinders, in the orientations shown, where the force acts in the direction of the arrows, for different ratios of the shortest distance between ends S to the length L , together with the corresponding predictions (lines). The data are for cylinders with aspect ratios between $L/\mathcal{R}=20$ and $L/\mathcal{R}=40$. All of the experimental data of Madani *et al.* (2010) have been divided by a factor of two.

391 The angle Ψ of motion relative to the force (figure 9b) does not provide a clear
 392 sense of how the cylinder moves. Figure 9(c) instead shows the angle of motion
 393 relative to the cylinder's own axis $((\pi/2) - \phi$; see figure 1a), which reveals that, close
 394 to the initiation of motion ($Od \rightarrow Od_c$) the cylinder slides almost along its axis for
 395 any inclination angle α greater than **approximately** $\pi/7$. Conversely, if the cylinder
 396 is oriented closer to the perpendicular ($\alpha \lesssim \pi/7$), it can drift in a wide range of
 397 directions. Both of these features are a consequence of the drag anisotropy for $Bi \gg 1$
 398 discussed in the previous section: the resistance to motion in the transverse direction
 399 is larger than that in the axial direction over almost the entire range of angles ϕ of
 400 motion relative to the axis.

401 Sedimentation of cylindrical rods was studied experimentally by Madani *et al.*
 402 (2010) in centrifuge experiments using Carbopol gel. They measured the critical force
 403 (i.e. $1/Od_c$) for the initiation of motion. Figure 10(a) shows their data for straight
 404 rods orientated either parallel ($\alpha = \pi/2$) or perpendicular ($\alpha = 0$) to the force against
 405 the aspect ratio of the rods, L/\mathcal{R} , where L is the rod length; our slender-body theory
 406 applies for $L \gg \mathcal{R}$. Like the theoretical predictions in (4.4), the two orientations lead
 407 to critical values of Od that are different by a factor of order unity (the factor is
 408 **approximately** 5 in the experimental data, and predicted theoretically to be close to 4).
 409 Curiously, however, both sets of experimental data are different from the theory by
 410 a factor of **approximately** two (this has been scaled out in the data in figure 10; see
 411 caption). We are not sure of the origin of this discrepancy, particularly since Tokpavi
 412 *et al.* (2009) report far better agreement with theory for their own experiments in the
 413 perpendicular orientation ($\alpha = 0$). Indeed, a separate set of experiments by Jossic &
 414 Magnin (2001) also measured the critical forces on cylinders in both the perpendicular
 415 and parallel orientation; their data are also shown (as stars) in figure 10(a), and **are**
 416 more consistent with the theoretical results.

417 We also performed our own simple experiments of the sedimentation of inclined
 418 rods, and the data are presented in figure 9(d). The experiments are conducted using

headless machine screws immersed in an aqueous Carbowol gel, as described in more detail in appendix D. The figure reports the sedimentation speed observed for screws of different size for varying orientation, distinguishing between rods that did or did not move over the duration of the experiments. This distinction picks out an estimate of the critical threshold Od_c , which compares well with the theoretical predictions. The screws in these experiments had aspect ratios L/\mathcal{R} lying between 13 and 33. Despite their simplicity, the experiments provide some other qualitative agreement with the predictions of the theory regarding the fall direction, although they also exhibit some potential sources of disagreement with the theory, as discussed in more detail in appendix D.

4.2.2. A bent rod

For a simple model of a bent rod, we assume that the axis is straight except for an abrupt corner at the midpoint, the effect of which on the flow dynamics is negligible. We further orientate the object so that the centreline is contained in a vertical plane and is symmetrical about the horizontal; i.e. we consider the two v-shaped orientations illustrated in figure 10(b). Thus, over half of the length of the rod the centreline makes an angle α with respect to the force, while over the other half the angle is equal and opposite. Such configurations were also examined by Madani *et al.* (2010) in their experimental study.

Figure 10(b) shows this experimental data together with the theoretical prediction for bent rods, with the degree of the bend measured in terms of the shortest distance between the ends of the rod S , divided by its original length L . As indicated in the plot, two symmetrical orientations are possible: a ‘scallop’ and a ‘v’ arrangement. When $S \rightarrow L$ the rods are straight, whereas for $S/L \rightarrow 0$ the rods become bent into two, potentially violating the slender-body assumptions (which leads us to truncate the plot at $S/L = 0.2$). Theoretically, the critical force depends only on the angle α , as was shown in figure 9(d). However, the two orientations differ in their definition of that angle, leading to the two curves in the figure: for the ‘scallop’ arrangement, $\alpha = \sin^{-1}(S/L)$, whereas $\alpha = \cos^{-1}(S/L)$ for the ‘v’ orientation. Once again, there is rough agreement between theory and experiment in terms of the dependence of Od_c on S/L , notwithstanding the same disconcerting factor of two.

4.3. Helices

For the flow around a turning and translating helix, we must again translate our computational results for the velocity field and drag relative to the local orientation of the filament. As illustrated in figure 1(b), we embed the helix inside a virtual cylindrical surface of radius \mathcal{R}_H , and let (s, t) denote axes that lie along and tangential to it. We further let Φ denote the pitch angle of the helix (i.e. the angle between the centre line of the filament and the t -axis). We first consider both sedimentation and locomotion of helices with arbitrary pitch angle (§§ 4.3.1 and 4.3.2), in which case the slender-body theory is valid when $\mathcal{R}_H \gg \mathcal{R}$. Then, in § 4.3.3, we consider locomotion driven by relatively long spiral waves with $\Phi \rightarrow \pi/2$; in this case the theory applies for $\mathcal{R}_H/\mathcal{R} = O(1)$.

The dimensional velocity $\mathcal{U}(\cos \phi, \sin \phi)$ associated with axes aligned with the filament corresponds to a translation speed \tilde{V}_s in the s -direction and a turning rate $\tilde{\omega}$ in the t -direction that are given by

$$\tilde{V}_s = -\mathcal{U} \cos(\phi + \Phi), \quad \tilde{\omega} = \frac{\mathcal{U}}{\mathcal{R}_H} \sin(\phi + \Phi). \quad (4.5a, b)$$

465 The dimensionless force on the helix is also resolved into the (s, t) -directions as

$$466 \begin{bmatrix} F_t \\ F_s \end{bmatrix} = \begin{bmatrix} F_z(\phi, Bi) \cos \Phi + F_x(\phi, Bi) \sin \Phi \\ F_z(\phi, Bi) \sin \Phi - F_x(\phi, Bi) \cos \Phi \end{bmatrix}. \quad (4.6)$$

4.3.1. The spiral of a sedimenting helix

467 When the helix is subjected to an axial force (in the s -direction), the helix drifts in
468 that direction along a spiral path. The force F_t is unbalanced and must therefore be
469 eliminated, which demands that

$$471 \Phi = -\tan^{-1} \left(\frac{F_z}{F_x} \right) = \pi - \alpha, \quad (4.7)$$

472 where the last equality follows from noting that both ϕ and α must lie in the range
473 $[\pi/2, \pi]$ in this scenario. As for the sedimenting rod, the dynamics is naturally
474 described in terms of the Oldroyd number (4.1). Hence we must transform the input
475 parameters from (ϕ, Bi) to $(\Phi, Od) \equiv (-\tan^{-1}(F_z/F_x), Bi/\sqrt{F_x^2 + F_z^2})$. The output
476 quantities are then the dimensionless fall speed and turn rate,

$$477 V_s = \frac{\mu \tilde{V}_s}{|\tilde{\mathbf{F}}|} = \frac{Od \cos[\phi(\Phi, Od) + \Phi]}{Bi(\Phi, Od)}, \quad \omega = \frac{\mu \mathcal{R}_H \tilde{\omega}}{|\tilde{\mathbf{F}}|} = \frac{Od \sin[\phi(\Phi, Od) + \Phi]}{Bi(\Phi, Od)}, \quad (4.8a,b)$$

479 shown in figure 11(a,b).

480 In the Newtonian limit $Bi \rightarrow 0$ (§ 3.1), the limiting drag components imply

$$481 (V_s, \omega) \sim \frac{\log Od^{-1}}{4\pi} (1 + \sin^2 \Phi, \sin \Phi \cos \Phi). \quad (4.9)$$

482 Conversely, for higher Od (weaker force) we again encounter a critical yield stress
483 Od_c above which there is no motion. Indeed, the critical stress $Od_c(\Phi)$ as a function
484 of pitch angle is the same as the critical stress $Od_c(\alpha)$ in terms of the inclination of
485 straight cylinders. Furthermore, the motion of the helix is affected by exactly the same
486 drag anisotropy as straight cylinders for $Od \rightarrow Od_c$ (see figure 11c). That is, for pitch
487 angles that are close to $\pi/2$ (i.e. for long loosely wound helices), the angle of motion
488 ϕ spans almost its full range, and so the spiral taken by any filament of the helix is
489 different from the curve itself. But for helices with $\Phi < \pi/2$, $\phi \rightarrow \pi/2$: the helix turns
490 such that each filament moves almost axially, and the helix falls via a corkscrewing
491 motion.

492 We performed a simple experiment of a sedimenting helix in Carbopol gel to
493 confirm the latter prediction, as shown in figure 12. The upper image shows the
494 helical corkscrew used, while the lower shows successive snapshots of the centreline
495 as the helix spirals vertically downwards (plotted to the right in the figure). As
496 illustrated by the near perfect alignment of the snapshots, the helix falls in almost the
497 direction of the filament axis to perform a corkscrew motion. Note that we are unable
498 to make any further quantitative comparison with theory as the Carbopol is better
499 modelled as a Herschel–Bulkley fluid rather than using the Bingham law (precluding
500 a direct comparison of the fall speed, for example). Nevertheless, the relatively slow
501 sedimentation speed (less than 1 cm min^{-1}), suggests that the helix is close to the
502 onset of motion. The Oldroyd number, however, is $Od = \tau_Y \mathcal{R}/(Mg) \approx 0.095$, which

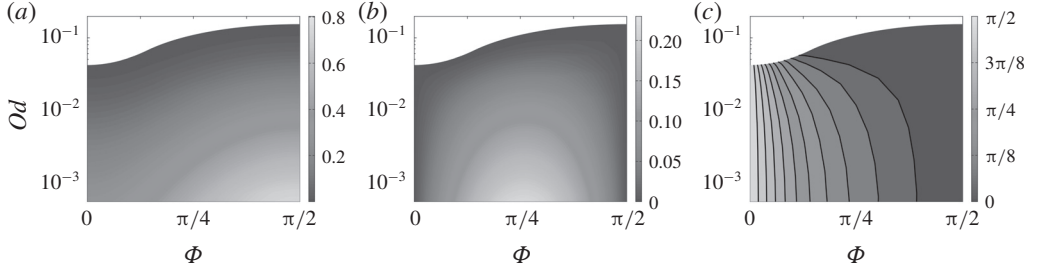


FIGURE 11. (Colour online) (a) The velocity V_s and (b) the angular rotation ω for helix with pitch Φ sedimenting along its axis. (c) The angle of motion $\phi - \pi/2$ of each filament of the helix to its own axial direction. Small angles indicate a nearly corkscrewing motion.

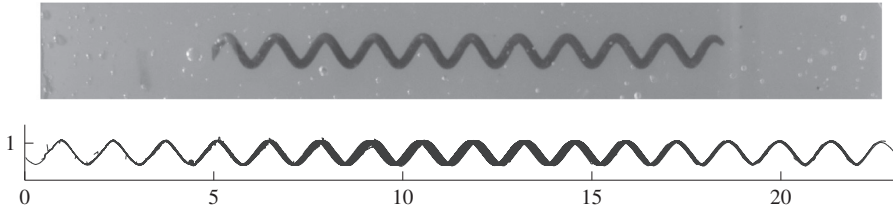


FIGURE 12. (Colour online) An image of a helix falling through Carbopol, and a plot showing successive snapshots of the centreline. The helix has mass $M \approx 10.6$ g, axial length 14 cm, radii $\mathcal{R} \approx 1.2$ mm and $\mathcal{R}_H \approx 3.4$ mm, pitch angle $\Phi \approx 32^\circ$, and falls vertically (to the right in the plots) with a speed of 0.83 cm min^{-1} .

is greater than the critical threshold of 0.083 for motion at the pitch angle of the corkscrew, $\Phi \approx 32^\circ = 0.18\pi$ rad. Given that the corkscrew is made of smooth steel, this discrepancy might point to a reduction of Od_c due to effective slip on its boundary (cf. Jossic & Magnin 2001). Alternatively, the radius of the helix $\mathcal{R}_H \approx 3.4$ mm is not that much larger than the filament radius $\mathcal{R} \approx 1.2$ mm, which suggests that the slender-body limit may be inaccurate.

4.3.2. Swimming with helical waves

In Taylor and Hancock's model of the locomotion of a micro-organism driven by helical waves propagating down a cylindrical flagellum (Taylor 1952; Hancock 1953), the filament spirals around the cylinder surface under the action of an imposed turning moment with $F_t \neq 0$, driving a swimming speed V_s . Force balance along the surface, however, now demands that the axial force F_s vanishes, or, given (4.6),

$$\Phi(\phi, Bi) = \tan^{-1} \left(\frac{F_x}{F_z} \right) \equiv \frac{\pi}{2} - \alpha. \quad (4.10)$$

In this situation, the imposed turning velocity $\mathcal{R}_H \tilde{\omega}$ provides a characteristic velocity scale. We therefore introduce a modified Bingham number,

$$Bi^* = \frac{\tau_Y \mathcal{R}}{\mu \mathcal{R}_H \tilde{\omega}} = \frac{Bi}{\sin(\phi + \Phi)}, \quad (4.11)$$

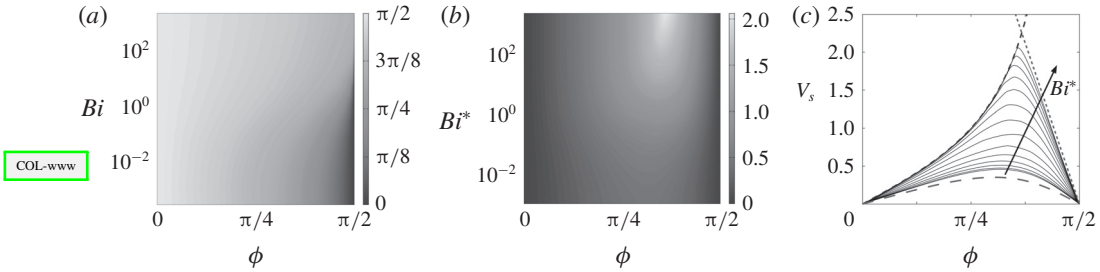


FIGURE 13. (Colour online) Calculations for a swimming cylindrical filaments propelled by helical waves. (a) The pitch angle $\Phi(\phi, Bi)$, calculated from (4.10). (b) The swimming speed $V_s(\Phi, Bi^*)$. (c) The swimming speed for different Bingham numbers between $Bi^* = 0.003$ and $Bi^* = 1995$, together with the Newtonian (red, long dashed) limit, the speed for perfect ‘corkscrewing’ (blue dashed) and the prediction for $\Phi \rightarrow \pi/2$ given in § 4.3.3 (for $\Omega \rightarrow 0$; green, short dashed).

519 given (4.5b), and write the dimensionless velocity along the cylindrical surface as

$$520 \begin{bmatrix} V_t \\ V_s \end{bmatrix} = \frac{1}{\mathcal{R}_H \tilde{\omega}} \begin{bmatrix} \tilde{V}_t \\ \tilde{V}_s \end{bmatrix} = \begin{bmatrix} 1 \\ -\cot(\phi + \Phi) \end{bmatrix}. \quad (4.12)$$

521 We now map the input parameters from (ϕ, Bi) to (Φ, Bi^*) , and then determine
522 the swimming speed $V_s(\Phi, Bi^*)$ from (4.12). Figure 13 shows the results of this
523 computation.

524 In the Newtonian limit ($Bi \rightarrow 0$ or $Bi^* \rightarrow 0$), we find that $\tan \alpha = (\tan \phi)/2 = \cot \Phi$,
525 given the limits in § 3.1. Hence

$$526 V_s \rightarrow \frac{\sin \Phi \cos \Phi}{1 + \cos^2 \Phi}, \quad (4.13)$$

527 which is equivalent to the result quoted by Hancock (1953).

528 For higher Bi^* , the swimming speed increases and, at a particular pitch angle,
529 attains a maximum that can exceed the turning velocity of the helix (i.e. $V_s > 1$; see
530 figure 13b,c). For pitch angles that are sufficiently below $\pi/2$, the speed converges
531 to the curve

$$532 V_s = \tan \Phi, \quad (4.14)$$

533 in the plastic limit $Bi^* \gg 1$ (figure 13c). This limit corresponds to a perfect
534 ‘corkscrewing’ motion, and follows from (4.12) with filaments of the helix moving
535 along their axis ($\phi = \pi/2$). The corkscrewing behaviour is once again a consequence
536 of the drag anisotropy $F_x > F_z$ outlined in § 4.1. When $Bi \gg 1$ (and hence $Bi^* \gg 1$), the
537 force angle α is small over most of the range of ϕ , and so, given (4.10), the pitch Φ
538 must be close to $\pi/2$. Hence variation in Φ away from $\pi/2$ must be accommodated
539 by a sensitive tuning of ϕ very near $\pi/2$. In other words, over much of the range of
540 pitch angles, ϕ is very close to $\pi/2$ and the filament translates almost along its axis
541 in a corkscrewing motion.

542 With a perfect corkscrewing motion, the swimming speed could in principle diverge
543 for pitch angles approaching $\pi/2$. As illustrated in figure 13(c), this is not achieved
544 for our model swimmer because, as Φ becomes closer to $\pi/2$, the angle ϕ is

redirected away from $\pi/2$. The swimming speed V_s thus deviates off the corkscrew curve (4.14) and decreases as Φ approaches $\pi/2$. The descent of the swimming speed corresponds to the main range of ϕ in the plots of the drag components (figure 8b,c), where $0 < \alpha \lesssim \pi/7$. Given this range of α , an optimal speed for $Bi \gg 1$ of $V_s \approx 2.14$ results from (4.14), at a pitch angle of $\Phi \approx 1.12$.

4.3.3. Long helical waves

When locomotion is driven by relatively long helical waves, the pitch of the helix is close to $\pi/2$ and the z -axis of the filament almost aligns with the s -axis of the helix. In this setting, we may assume that $\mathcal{R}_H/\mathcal{R} = O(1)$. In the local Cartesian coordinates of the filament, the rigid turning and translation of the helix driven by angular rotation $\tilde{\omega}$ then provides the dimensional surface velocity field,

$$(\mathcal{R}_H - \mathcal{R} \sin \theta) \tilde{\omega} \hat{x} + \mathcal{R} \cos \theta \tilde{\omega} \hat{y} + W \hat{z} \equiv \mathcal{U}(\cos \theta \cos \phi, \Omega - \sin \theta \cos \phi, \sin \phi), \quad (4.15)$$

where $W = \tilde{V}_s$ is the dimensional locomotion speed. The latter expression in (4.15) is simply a dimensional version of the generic boundary condition in (2.7), where $\mathcal{U} = \sqrt{U^2 + W^2}$ as before but now

$$U = \mathcal{R}_H \tilde{\omega} \quad \text{and} \quad \Omega = \frac{\mathcal{R} \tilde{\omega}}{\mathcal{U}}. \quad (4.16a,b)$$

In this long wave limit, the condition $\Phi \rightarrow \pi/2$ is expected to demand that $\phi \ll 1$ (cf. figure 13), and so the surface velocity (4.15) is

$$\mathcal{U}(\cos \theta, \Omega - \sin \theta, \phi), \quad (4.17)$$

with

$$\frac{W}{\mathcal{U}} = V_s \approx \phi, \quad \mathcal{U} \approx \mathcal{R}_H \tilde{\omega} \quad \text{and} \quad \Omega \approx \frac{\mathcal{R}}{\mathcal{R}_H}. \quad (4.18a-c)$$

Solutions in this limit can therefore be calculated by computing the motion of a cylinder at small ϕ , but with arbitrary rotation rate Ω , to determine the drag force,

$$F_x(\phi, \Omega, Bi) \hat{x} + F_z(\phi, \Omega, Bi) \hat{z} \approx F_x(0, \Omega, Bi) \hat{x} + \phi F'_z(\Omega, Bi) \hat{z}, \quad (4.19)$$

with

$$F'_z(\Omega, Bi) \equiv \left[\frac{\partial}{\partial \phi} F_z \right]_{\phi=0}. \quad (4.20)$$

But, as before, $\alpha = (\pi/2) - \Phi$, and so

$$\phi(\Omega, Bi) \approx \left(\frac{1}{2} \pi - \Phi \right) \frac{F_x(0, \Omega, Bi)}{F'_z(\Omega, Bi)}, \quad (4.21)$$

which is the dimensionless swimming speed. Note that, in the Newtonian limit, the results in (3.1) imply that $\phi \sim 2((\pi/2) - \Phi)$, which is equivalent to the $\Phi \rightarrow \pi/2$ limit of (4.13).

Figure 14(a) shows computations of the speed coefficient $F_x(0, \Omega, Bi)/F'_z(\Omega, Bi)$ for varying radius ratio Ω and different yield stresses. For $\Omega \rightarrow 0$, the helix is loosely

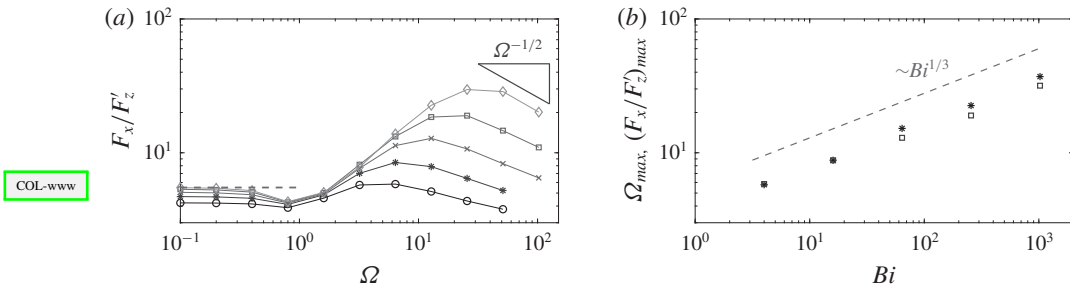


FIGURE 14. (Colour online) (a) Computations of the speed coefficient $F_x(0, \Omega, Bi)/F'_z(\Omega, Bi)$ in (4.21) for varying Ω and $Bi = 4$ (black circles), $Bi = 16$ (blue stars), $Bi = 64$ (red crosses), $Bi = 256$ (green squares) and $Bi = 1024$ (grey diamonds), together with the high- Bi limit for $\Omega = 0$ from the data in figure 8 (red dashed). (b) The (interpolated) maximum speed coefficient $(F_x/F'_z)_{max}$ (blue squares) and corresponding Bingham number at which it is attained Bi_{max} (black stars).

wound and (4.21) reduces to the $\Phi \rightarrow \pi/2$ limit of the analysis in §4.3.2. The speed increases towards a maximum value when the helix is more tightly wound (larger Ω), before decreasing again towards zero as $\Omega \rightarrow \infty$.

In the loosely wound limit, the swimming speed is insensitive to the radius ratio and approaches a finite value for large yield stress. One expects this result for $Bi \gg 1$ because the stress fields of the underlying plasticity solutions are independent of Ω until the rotation rate becomes sufficiently large to force a change in the slipline pattern (see §3.3.2). In addition, when the flow pattern contains a significant nearly perfectly plastic region, the stresses, and therefore the drag components, are all expected to scale with Bi , such that the speed is independent of Bi in the plastic limit. Only when the plastic flow outside the cylinder is replaced by a boundary-layer flow for larger Ω (see §3.3.2 and figure 4) does the speed becomes more strongly dependent on the yield stress. In this very tightly wound limit, the transverse drag is $F_x \sim Bi^{3/2} \Omega^{-3/2}$ (see §3.3.2), while the axial drag scales with $F_z \sim \phi Bi \Omega^{-1}$, because $\tau_{rz} \sim Bi w_r/|v_r| \sim O(\phi Bi/\Omega)$. Hence, $\phi \sim Bi^{1/2} \Omega^{-1/2}$, which captures the final decay of the swimming speed for $\Omega \gg 1$ in figure 14(a). A maximum value of the speed is attained between these two limits, for $O(1) < \Omega < O(Bi^{1/3})$, where the axial drag decays like $F_z \sim \phi Bi \Omega^{-1}$ but the stress state is still given by the modified slipline solution in §3.3.2 and the transverse drag remains $O(Bi)$. The speed grows over this intermediate range, and attains a maximum value $(F_x/F'_z)_{max} \sim Bi^{1/3}$ when $\Omega = \Omega_{max} \sim Bi^{1/3}$ (figure 14b).

5. Summary

In this paper we have formulated viscoplastic slender-body theory to describe the slow (inertialless) flow of a yield-stress fluid around a thin cylindrical filament. For Newtonian Stokes flow, the linearity of the problem means that a general solution can be found by breaking things down into the constituent components of motion (transverse and axial motion plus rotation) and then suitably superposing the results. The nonlinearity of the constitutive law means that such a superposition is not possible here, forcing us to consider all the possible combinations independently. The theory does, however, simplify matters by exploiting the slenderness of the filament to reduce the problem to that of the local flow around a cylinder, which is inclined relative

to its direction of motion and rotates. We solved this problem numerically using a specially designed technique to deal with the yield stress (an augmented Lagrangian scheme). We also provided some exact or asymptotic solutions in different analytically accessible limits.

We applied the theory to the sedimentation of a straight or bent rod, and compared the results with both existing experiments (Jossic & Magnin 2001; Tokpavi *et al.* 2009; Madani *et al.* 2010) and some simple experiments of our own. We further considered flow around a helix, by exploring both the spiral fall of a vertical helix and the locomotion of a cylindrical filament driven by helical waves. The latter makes a non-Newtonian generalization of the model of Taylor (1952) and Hancock (1953) for a swimming microscopic organism with a flagellum. We found that, as the strength of the yield stress increases, an optimal swimming speed arises for a certain pitch angle of the helix, which is connected to a near corkscrewing motion of the helix. This results because the drag opposing transverse motion is typically higher than that opposing axial motion, and may have application to biological organisms such as spirochetes that are observed to perform a corkscrewing motion in gel-like materials (Wolgemuth *et al.* 2006).

Acknowledgements

We thank J. Lister, M. Martinez and G. Peng for helpful comments.

Appendix A. Two-dimensional viscoplastic boundary-layer theory

As suggested by Piau (2002) and confirmed by Tokpavi *et al.* (2008), the boundary layers against the solid surface of the cylinder in the limit of transverse motion have a thickness of $O(Bi^{-1/2})$. As predicted by Oldroyd (1947) and shown by Balmforth *et al.* (2017), on the other hand, the free viscoplastic shear layers have a thickness of $O(Bi^{-1/3})$ and a structure with self-similar form. For a shear layer with a curving centreline, however, the theory outlined by Balmforth *et al.* (2017) is strictly only valid when the curvature $\kappa \ll O(1)$ (despite an erroneous statement to the contrary contained in that paper). In this appendix, we briefly outline the correct generalization to order-one curvatures.

We resolve the boundary layer in terms of a local coordinate system $(s, n = \epsilon\eta)$ based on arc length s and a stretched transverse coordinate η , and introduce the velocity field $(\mathcal{U}, \epsilon\mathcal{V})$, where $\epsilon = Bi^{-1/3}$. The force balance can then be expressed as

$$\epsilon \frac{\partial \tau_{ss}}{\partial s} + (1 - \epsilon\kappa\eta) \frac{\partial \tau_{sn}}{\partial \eta} - 2\epsilon\kappa\tau_{sn} = \epsilon \frac{\partial p}{\partial s}, \quad (\text{A } 1)$$

$$\epsilon \frac{\partial \tau_{sn}}{\partial s} + (1 - \epsilon\kappa\eta) \frac{\partial \tau_{nn}}{\partial \eta} + \epsilon\kappa(\tau_{ss} - \tau_{nn}) = \frac{\partial p}{\partial \eta}. \quad (\text{A } 2)$$

The components of the deformation rate tensor scale as

$$\dot{\gamma}_{ss} = \frac{2}{1 - \epsilon\kappa\eta} \left(\frac{\partial \mathcal{U}}{\partial s} - \epsilon\kappa\mathcal{V} \right), \quad \dot{\gamma}_{nn} = 2 \frac{\partial \mathcal{V}}{\partial \eta}, \quad \dot{\gamma}_{sn} = \frac{1}{1 - \epsilon\kappa\eta} \left(\epsilon \frac{\partial \mathcal{V}}{\partial s} + \kappa\mathcal{U} \right) + \frac{1}{\epsilon} \frac{\partial \mathcal{U}}{\partial \eta}, \quad (\text{A } 3a-c)$$

which, in view of the constitutive law, $\tau_{ij} = \dot{\gamma}_{ij}(1 + \epsilon^{-3}\dot{\gamma}^{-1})$, guide the stress scalings, $\tau_{sn} = \epsilon^{-3} \text{sgn}(\mathcal{U}_\eta) + \epsilon^{-1} \check{\tau}_{sn}(s, \eta)$ and $(\tau_{ss}, \tau_{nn}) = O(\epsilon^{-2})$. To account for the third term

648 on the left of (A 1) and maintain a consistent balance in that equation at $O(\epsilon^{-1})$, we
 649 now introduce the pressure scaling,

$$650 \quad p = \mp \frac{2}{\epsilon^3} \vartheta + \frac{1}{\epsilon^2} P(s, \eta), \quad (\text{A } 4)$$

651 where $\vartheta(s)$ is the angle that the **centreline** of the boundary layer makes with the
 652 x -axis, so that $\kappa = \partial\vartheta/\partial s$. The first term in the pressure solution (A 4), which is
 653 missing in Balmforth *et al.* (2017), reflects how $p \pm 2Bi\vartheta$ is, to leading order, constant
 654 along the boundary layer. But that centreline must be equivalent to a slipline, and
 655 $p \pm 2Bi\vartheta$ is simply the corresponding Riemann invariant. With this correction to the
 656 pressure solution, the remainder of the **boundary-layer** theory proceeds as outlined by
 657 Balmforth *et al.* (2017).

658 Appendix B. Sliplines for rotating and translating cylinders

659 The notation in this appendix refers to figure 3(b). Let Θ denote the angle of the
 660 line BC , and p_0 the pressure at the base of the fan. Since the circles of the fan are
 661 β -lines, and $\vartheta = -\pi/2$ along the α -line $x = 0$, the pressure within the fan is $p =$
 662 $p_0 + 2Bi\vartheta + \pi Bi$. It follows that the pressure along BC is $p = p_0 + (\pi + 2\Theta)Bi$. The
 663 circular failure arc CD is an α -line with pressure $p = p_0 + (\pi + 4\Theta - 2\vartheta)Bi$. Along
 664 CD (with $\vartheta = 2\pi - \Theta$) we therefore have $p = p_0 - (3\pi - 6\Theta)Bi$, implying that the
 665 pressure in the fan must be $p = p_0 + 2Bi\vartheta - (7\pi - 8\Theta)Bi$. On returning to the α -line
 666 $x = 0$ cutting through the base of the fan (now with $\vartheta = 2\pi + (\pi/2)$), we therefore
 667 find the pressure $p = p_0 - 2(\pi - 4\Theta)Bi$. Eliminating the pressure drop then demands
 668 that $\Theta = \pi/4$.

669 In $x > 0$, the involutes of circles that extend the β -lines from the centred fan above
 670 $y = -1$ can be taken to have the parametric form, $x = \sin \vartheta + (a - \vartheta) \cos \vartheta$ and
 671 $y = (a - \vartheta) \sin \vartheta - \cos \vartheta$, where a is the horizontal location of the curve along $y = -1$
 672 (with $\vartheta = 0$), which also determines the polar angle $\theta = (\pi/2) - a$ at the intersection
 673 with the cylinder (where $\vartheta = a$). Given that the α -line BC has $\vartheta = \pi/4$, the geometry
 674 demands that the radius of the rigidly rotating plug is $R = 1 + (y_0\sqrt{2}/2)$, and that of
 675 the centred fan is $(\pi/4) + (y_0\sqrt{2}/2)$.

676 We now quote the local force and torque along the closed contour $ABCDEA$, whose
 677 integrals set the total force and torque upon the cylinder (without inertia, there can be
 678 no net force or torque on the rigid plug attached to the cylinder). A key feature of
 679 this computation is that along the sliplines the normal force is given by the pressure p
 680 and the tangential (anti-clockwise) force is the shear stress $-Bi$. Thus, the local force
 681 and torque in a line element of length ds are

$$682 \quad \mathbf{f} = \begin{pmatrix} -Bi \cos \vartheta - p \sin \vartheta \\ -Bi \sin \vartheta + p \cos \vartheta \end{pmatrix} ds \quad \text{and} \quad \mathbf{r} \times \mathbf{f}, \quad (\text{B } 1a,b)$$

683 where the position vector \mathbf{r} , pressure p and line element ds break down into

$$684 \quad AB: \quad \mathbf{r} = \begin{pmatrix} \sin \vartheta \\ -\cos \vartheta \end{pmatrix}, \quad p = p_0 + (\pi + 2\vartheta)Bi, \quad ds = d\vartheta, \quad 0 < \vartheta < \frac{1}{4}\pi; \quad (\text{B } 2)$$

$$685 \quad BC: \quad \mathbf{r} = \frac{1}{\sqrt{2}} \begin{pmatrix} s + 1 \\ s - 1 \end{pmatrix}, \quad p = p_0 + \frac{3}{2}\pi Bi \quad \vartheta = \frac{1}{4}\pi, \quad 0 < s < \frac{1}{2}y_0\sqrt{(2)}; \quad (\text{B } 3)$$

$$CD: \quad \mathbf{r} = \begin{pmatrix} R \sin \vartheta \\ y_0 - R \cos \vartheta \end{pmatrix}, \quad p = p_0 + 2(\pi - \vartheta)Bi, \quad ds = R d\vartheta, \quad \frac{1}{4}\pi < \vartheta < \frac{7}{4}\pi; \quad (B 4)$$

$$DE: \quad \mathbf{r} = \frac{1}{\sqrt{2}} \begin{pmatrix} s - 1 \\ -s - 1 \end{pmatrix}, \quad p = p_0 - \frac{3}{2}\pi Bi \quad \vartheta = \frac{7}{4}\pi, \\ -\frac{1}{2}y_0\sqrt{(2)} < s < 0; \quad (B 5)$$

$$EA: \quad \mathbf{r} = \begin{pmatrix} \sin \vartheta \\ -\cos \vartheta \end{pmatrix}, \quad p = p_0 - (5\pi - 2\vartheta)Bi, \quad ds = d\vartheta, \quad \frac{7}{4}\pi < \vartheta < 2\pi. \quad (B 6)$$

These furnish the net force and torque quoted in the main text.

Appendix C. Translation inside the axial yield surface

When flow is contained within the yielded region generated by axial motion, for $(\pi/2) - \phi = \delta \ll 1$, we have the axial velocity field given in § 3.2: $w \sim 1 + Bi(r - 1 - r_p \log r)$. Let $(\phi - (\pi/2), u, v) = \delta(1, u_1, v_1) + \dots$, $w = w_0(r) + \delta^2 w_2$ and $(u_1, v_1) = (\psi_\theta/r, -\psi_r)$. Then,

$$\tau_{rz} \sim -Bi \frac{r_p}{r} + \delta^2 \left(w_{2r} + \frac{Bi \dot{\gamma}_\perp^2}{2w_{0r}^2} \right), \quad \tau_{\theta z} \sim \frac{\delta^2 r_p w_{2\theta}}{r(r_p - r)}, \quad (C 1a,b)$$

$$\begin{pmatrix} \tau_{rr} \\ \tau_{r\theta} \end{pmatrix} \sim \frac{r_p}{r_p - r} \begin{pmatrix} 2(\psi_\theta/r)_r \\ \psi_r/r - \psi_{rr} + \psi_{\theta\theta}/r^2 \end{pmatrix} \quad (C 2)$$

and

$$\dot{\gamma}^2 \sim (w_{0r} + \delta^2 w_{2r})^2 + \delta^2 \dot{\gamma}_\perp^2, \quad \dot{\gamma}_\perp^2 \equiv 4(\psi_\theta/r)_r^2 + (\psi_{rr} - \psi_r/r - \psi_{\theta\theta}/r^2)^2. \quad (C 3a,b)$$

The boundary conditions at $r = 1$ still imply $w_2 = 0$ and $(\psi_\theta, -\psi_r) = (\cos \theta, -\sin \theta)$, but the corrections perturb the position of the plug to $r = r_p + \delta^2 r_{p2}$. Given that $u = v = w = 0$ and $\dot{\gamma} = 0$ on this boundary, an expansion about $r = r_p$ furnishes

$$w_2 = w_{2r} + r_{p2} w_{0rr} = \psi = \psi_r = \dot{\gamma}_\perp^2 = 0 \quad \text{at } r = r_p. \quad (C 4)$$

After eliminating the pressure from the planar **force-balance** equations, we find

$$\left[\frac{\partial}{\partial r} \frac{1}{r} \frac{\partial}{\partial r} \frac{r^2}{(r_p - r)} \frac{\partial}{\partial r} - \frac{4}{r} \frac{\partial}{\partial r} \frac{1}{(r_p - r)} + \frac{1}{r(r_p - r)} \frac{\partial}{\partial r} \right] r \frac{\partial}{\partial r} \left(\frac{\Psi}{r} \right) = 0, \quad (C 5)$$

given that a separable solution is possible with $\psi = \Psi(r) \sin \theta$, $\Psi(1) = \Psi_r(1) = 1$ and $\Psi(r_p) = \Psi_r(r_p) = 0$. At the following order, the axial problem gives

$$(r w_{2r})_r + \frac{r_p}{r(r_p - r)} w_{2\theta\theta} = - \left[\frac{r^3 \dot{\gamma}_\perp^2}{2Bi(r_p - r)^2} \right]_r, \quad (C 6)$$

with $w_2(1, \theta) = w_2(r_p, \theta) = 0$ and $r_{p2} = -r_p w_{2r}(r_p, \theta)/Bi$, illustrating how the lateral translation perturbs the axial flow and yield surface.

For $Bi \gg 1$, the solution is more directly obtained and explicit: the axial velocity is

$$w \sim (1 - \xi)^2, \quad r = 1 + Bi^{-1/2} \xi \sqrt{2}. \quad (C 7a,b)$$

718 Continuity, planar force balance and the constitutive law demand that, at leading
719 order,

$$720 \frac{Bi^{1/2}}{\sqrt{2}} u_\xi + v_\theta \sim 0, \quad \frac{\partial p}{\partial \xi} \sim 0 \quad \text{and} \quad \frac{\partial p}{\partial \theta} \sim \frac{Bi^{1/2}}{\sqrt{2}} \frac{\partial}{\partial \xi} \tau_{r\theta} \sim \frac{Bi^{3/2}}{2\sqrt{2}} \left(\frac{v_\xi}{1-\xi} \right)_\xi, \quad (\text{C } 8a-c)$$

721 with boundary conditions, $u = \delta \cos \theta$ and $v \sim 0$ at $\xi = 0$, and $(u, v) = (0, 0)$ at $\xi = 1$.
722 Various integrals therefore give

$$723 u = (1 - \xi)^3 (1 + 3\xi) \delta \cos \theta \quad \text{and} \quad v = 6\sqrt{2} Bi^{1/2} \xi (1 - \xi)^2 \delta \sin \theta. \quad (\text{C } 9a,b)$$

724 It follows that the pressure is $p \sim 9Bi^2 \delta \cos \theta$, and the drag force is

$$725 F_x \sim \frac{Bi^{1/2}}{\sqrt{2}} \oint \left[\frac{\partial \tau_{r\theta}}{\partial \xi} \right]_{\xi=0} d\theta \sim - \oint p \cos \theta d\theta \sim -9\pi Bi^2 \delta \quad (\text{C } 10)$$

726 (see figure 8d). The $\delta^2 w_2$ correction (C 7) now satisfies

$$727 w_{2\xi\xi} \sim -9\sqrt{2} B^{3/2} [(1 - 3\xi)^2]_\xi \sin^2 \theta. \quad (\text{C } 11)$$

728 Hence, given $w_2 = 0$ at $\xi = 0$ and 1,

$$729 w \sim (1 - \xi)^2 + 27\sqrt{2} \delta^2 Bi^{3/2} \xi^2 (1 - \xi) \sin^2 \theta, \quad (\text{C } 12)$$

730 which implies a shift in the yield surface of

$$731 r_p \sim 1 + Bi^{-1/2} (\sqrt{2} + 27\delta^2 Bi^{3/2} \sin^2 \theta). \quad (\text{C } 13)$$

732 Note that the pressure solution $p \sim 9Bi^2 \delta \cos \theta$ is only much less than $O(Bi)$
733 when $\delta \ll Bi^{-1}$. For $\delta > O(Bi^{-1})$, the continuity of the axially varying pressure into
734 the region outside the boundary layer and the force balance suggest that the stress
735 components cannot remain below the yield stress, regardless of the indeterminacy of
736 the stress state if $\tau < Bi$. In other words, once the angle ϕ becomes further from
737 $\pi/2$, the stress exerted by the boundary-layer flow must force the fluid to yield over
738 an order-one region beyond.

739 The flow pattern which then emerges combines the boundary layer around the
740 cylinder in which the axial velocity mostly remains localized, with an almost perfectly
741 plastic region beyond, as seen in figure 6(i). As $r \rightarrow 1$, the outer plastic flow satisfies
742 the stress conditions $\tau_{rz} \rightarrow -Bi$ with all other $\tau_{ij} \rightarrow 0$, and is forced purely by the
743 radial velocity of the cylinder $u \rightarrow \delta \cos \theta$, tolerating an arbitrary slip in v and w .
744 The plastic flow speeds are therefore $O(\delta)$, with $O(Bi)$ deviatoric stress components
745 and pressure.

746 Although the boundary layer retains the $O(Bi^{-1/2})$ thickness of the planar
747 viscoplastic boundary-layer problem (appendix A), it is dominated by the axial
748 shear stress $\tau_{rz} \sim -Bi$ rather than the planar component $\tau_{r\theta}$. It follows that, to $O(\delta)$,
749 the axial velocity profile is again given by (C 7). Moreover, the planar boundary-layer
750 equations in (C 8) remain valid, but with continuity with the outer plastic flow
751 demanding that $p = O(Bi)$. Thus, $\tau_{rz} \sim Bi v_\xi / |w_\xi| = O(Bi^{1/2})$, and the angular velocity
752 is $v = O(Bi^{-1/2})$, which greatly exceeds $O(\delta)$ cylinder motion for $\delta \ll O(Bi^{-1/2})$.
753 However, the contribution of the boundary-layer flow to the radial velocity is $O(Bi^{-1})$
754 and cannot correct the leading-order term $u \sim \delta \cos \theta$ due to the cylinder motion
755 if $\delta \gg O(Bi^{-1})$. Thus, for $1 \gg \delta \gg O(Bi^{-1})$, $F_z \sim -2\pi Bi$ and F_x is dictated by the
756 $O(Bi)$ pressure distribution stemming from the outer $O(\delta)$ plastic flow (cf. figure 8c).
757 Evidently, when $\delta = O(Bi^{-1})$ the boundary-layer flow adjusts the radial velocity and
758 consumes the outer plastic flow.

Appendix D. Sedimentation experiments

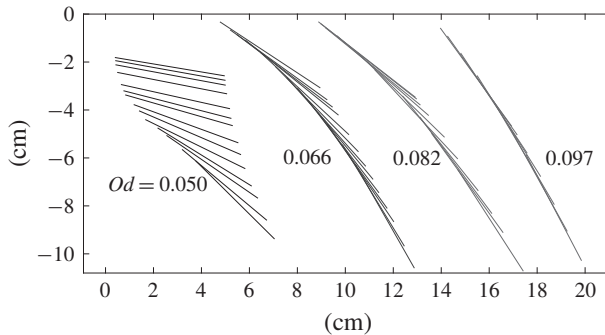
For a laboratory study of the fall of inclined rods, we conducted experiments using headless machine screws immersed in an aqueous solution of Carbopol Ultrez 21 (concentration of approximately 0.5% by weight, neutralized with sodium hydroxide). The screws had lengths of $L \approx 4.9$ cm and varying maximum radius \mathcal{R} , ranging from 1.5 to 3.9 mm. A Herschel–Bulkley fit to the flow curve measured in a rheometer (MCR501, Anton Paar, with roughened parallel plates) suggested a yield stress of approximately 38 Pa. The Carbopol was placed in a small tank (length 33 cm, depth 12 cm and width 5 cm), the screws introduced at varying orientations, and the fluid surface levelled with a scraper. A camera took photographs of the fall of the screws, and the time-dependent position of the centre was extracted from the images.

In experiments of this kind, one practical concern is that effective slip may occur over the surface of a smooth rod (e.g. Poumaere *et al.* 2014; Jalaal, Balmforth & Stoeber 2015) and thereby change the sedimentation dynamics. This motivated our use of steel screws for which the grooved surface, though complicating the detailed geometry, likely clogs up with Carbopol. A no-slip condition is thereby introduced at a position close to the maximum radius of the screw \mathcal{R} . The clogged Carbopol slightly modifies the effective mass of the rod: if the screw originally has mass M , and assuming that the grooves are fully clogged, the effective mass can be estimated as

$$M^* = M \left(1 - \frac{\rho_c}{\rho_s} \right) + \pi \rho_c \mathcal{R}^2 L, \quad (\text{D } 1)$$

where ρ_c and ρ_s are the density of Carbopol and steel, respectively (1 and 8 g cm⁻³). The adjusted Oldroyd number is $Od = \tau_Y \mathcal{R} L / (M^* g)$.

If the screw had not noticeably fallen over a time of approximately 10³ s, that inclination of the rod was noted as being below the critical value Od_c . Otherwise, the fall speed was measured as a function of orientation angle from consecutive images. There are a number of potential issues with these measurements: although the geometry of the screw may eliminate slip, the object is not truly cylindrical and small bubbles can become trapped on the surface. The screws also have finite length, which potentially introduces additional dynamical effect from the ends. More awkwardly, Carbopol is known to have a non-ideal rheology that may affect sedimentation (Tabuteau, Coussot & de Bruyn 2007; Putz *et al.* 2008). Finally, the flow curve measured in the rheometer may not provide a particularly accurate estimate of the yield stress (even were there a unique value for this property). These issues potentially explain a significant amount of scatter in the measurements of fall speed. They may also contribute to another observed effect: the gradual tilting of the screws towards the vertical as they fall. This effect, which is illustrated in figure 15, is not expected in our $Re \rightarrow 0$ theory, and may well have an inertial origin: the slower, lighter rods re-orientate less than the faster, heavier ones. From an experimental perspective, the tilt is convenient, allowing multiple speed values for different inclinations to be extracted during a single fall. Aside from this effect, and in agreement with theoretical predictions, rods with appreciable inclinations fall nearly along their axes, whereas almost horizontal rods fall in a wider range of directions.



COL-www

FIGURE 15. (Colour online) Snapshots (unequally spaced in time) of the centrelines of the four heaviest screws during sample falls. The spacing in time was roughly inversely proportional to the fall speed (cf. figure 9d), and ranged from a few hundred seconds for the less tilted screws to a few seconds at higher inclinations.

REFERENCES

- 802
- 803 BALMFORTH, N. J., CRASTER, R. V., HEWITT, D. R., HORMOZI, S. & MALEKI, A. 2017
 804 Viscoplastic boundary layers. *J. Fluid Mech.* **813**, 929–954.
- 805 GRAY, J. & HANCOCK, G. J. 1979 The propulsion of sea-urchin spermatozoa. *Biophys. J.* **25**, 113–127.
- 806 HANCOCK, G. J. 1953 The self-propulsion of microscopic organisms through liquids. *Proc. R. Soc.*
 807 *Lond. A* **217**, 96–121.
- 808 HEWITT, D. R. & BALMFORTH, N. J. 2017 Taylor’s swimming sheet in a yield-stress fluid. *J. Fluid*
 809 *Mech.* **828**, 33–56.
- 810 HINCH, E. J. 1991 *Perturbation Methods*. Cambridge University Press.
- 811 HOSOI, A. E. & GOLDMAN, D. I. 2015 Beneath our feet: strategies for locomotion in granular
 812 media. *Annu. Rev. Fluid Mech.* **47**, 431–453.
- 813 JALAAL, M., BALMFORTH, N. J. & STOEBER, B. 2015 Slip of spreading viscoplastic droplets.
 814 *Langmuir* **31**, 12071–12075.
- 815 JOSSIC, L. & MAGNIN, A. 2001 Drag and stability of objects in a yield stress fluid. *AIChE J.* **47**,
 816 2666–2672.
- 817 KELLER, J. B. & RUBINOW, S. I. 1976 Slender-body theory for slow viscous flow. *J. Fluid Mech.*
 818 **75** (4), 705–714.
- 819 LAMB, H. 1932 *Hydrodynamics*. Cambridge University Press.
- 820 LAUGA, E. & POWERS, T. R. 2009 The hydrodynamics of swimming microorganisms. *Rep. Prog.*
 821 *Phys.* **72** (9), 096601.
- 822 LIGHTHILL, S. J. 1975 *Mathematical Biofluidynamics*. SIAM.
- 823 MADANI, A., STOREY, S., OLSON, J. A., FRIGAARD, I. A., SALMELA, J. & MARTINEZ, D. M.
 824 2010 Fractionation of non-Brownian rod-like particle suspensions in a viscoplastic fluid. *Chem.*
 825 *Engng Sci.* **65** (5), 1762–1772.
- 826 OLDROYD, J. G. 1947 Two-dimensional plastic flow of a Bingham solid: a plastic boundary-layer
 827 theory for slow motion. *Proc. Camb. Phil. Soc.* **43**, 383–395.
- 828 PIAU, J.-M. 2002 Viscoplastic boundary layer. *J. Non-Newtonian Fluid Mech.* **102**, 193–218.
- 829 POUMAERE, A., MOYERS-GONZÁLEZ, M., CASTELAIN, C. & BURGHELEA, T. 2014 Unsteady
 830 laminar flows of a Carbopol gel in the presence of wall slip. *J. Non-Newtonian Fluid Mech.*
 831 **205**, 28–40.
- 832 PUTZ, A. M. V., BURGHELEA, T. I., FRIGAARD, I. A. & MARTINEZ, D. M. 2008 Settling of an
 833 isolated spherical particle in a yield stress shear thinning fluid. *Phys. Fluids* **20** (3), 033102.
- 834 RANDOLPH, M. F. & HOULSBY, G. T. 1984 The limiting pressure on a circular pile loaded laterally
 835 in cohesive soil. *Géotechnique* **34**, 613–623.

- ROQUET, N. & SARAMITO, P. 2003 An adaptive finite element method for Bingham fluid flows around a cylinder. *Comput. Meth. Appl. Mech. Engng* **192**, 3317–3341. 836
- SARAMITO, P. & WACHS, A. 2017 Progress in numerical simulation of yield stress fluid flows. *Rheol. Acta* **56**, 211–230. 837
- TABUTEAU, H., COUSSOT, P. & DE BRUYN, J. R. 2007 Drag force on a sphere in steady motion through a yield-stress fluid. *J. Rheol.* **51**, 125–137. 838
- TAYLOR, G. I. 1952 The action of waving cylindrical tails in propelling microscopic organisms. *Proc. R. Soc. Lond. A* **211**, 225–239. 839
- TOKPAVI, D. L., MAGNIN, A. & JAY, P. 2008 Very slow flow of Bingham viscoplastic fluid around a circular cylinder. *J. Non-Newtonian Fluid Mech.* **154**, 65–76. 840
- TOKPAVI, D. L., MAGNIN, A., JAY, P. & JOSSIC, L. 2009 Experimental study of the very slow flow of a yield stress fluid around a circular cylinder. *J. Non-Newtonian Fluid Mech.* **164**, 35–44. 841
- TORNBERG, A.-K. & SHELLEY, M. J. 2004 Simulating the dynamics and interactions of flexible fibers in Stokes flows. *J. Comput. Phys.* **196** (1), 8–40. 842
- WOLGEMUTH, C. W., CHARON, N. W., GOLDSTEIN, S. F. & GOLDSTEIN, R. E. 2006 The flagellar cytoskeleton of the spirochetes. *J. Mol. Microbiol. Biotechnol.* **11**, 221–227. 843
- 844
- 845
- 846
- 847
- 848
- 849
- 850
- 851

Please do not answer on this page but find the appropriate point in the text and make your annotation there.

Author Queries

Journal: FLM
Article id: 00726
Author: D. R. Hewitt and N. J. Balmforth
Short title: Viscoplastic slender-body theory

Q1 (Page 1)

Au: The distinction between surnames can be ambiguous, therefore to ensure accurate tagging for indexing purposes online (eg for PubMed entries), please check that the highlighted surnames have been correctly identified, that all names are in the correct order and spelt correctly.

Q2 (Page 1)

Au: Please check that the affiliations are correct for all authors. Also please ensure that department, institution, town, postal code and country are included if missing.

Q3 (Page 1)

Au: As per journal style only 1–3 key words are required. Please retain up to three. Key words must be selected from the list available at <http://journals.cambridge.org/data/relatedlink/jfm-keywords.pdf>

Q4 (Page 23)

Au: The journals style for vectors is to use bold italic (e.g. \mathbf{d}), and the style for matrices and tensors is to use bold sloping sanserif (e.g. \mathbf{W} ; \mathbf{D}). (However, when matrices involve Greek symbols, bold italic is used.) The components of these stay light italic for vectors and light sloping sans serif (e.g. T) for matrices and tensors. Please check that these have been used correctly and consistently in line with the journals preferences, and mark all changes on your proof.